https://doi.org/10.5194/egusphere-2026-724
Preprint. Discussion started: 31 March 2026

From point cloud to digital elevation model: Airborne topo-bathymetric LiDAR processing over the 28 km Ardèche River Gorges

Ron Nativ[1*], Dimitri Lague[1,2], Paul Leroy[2], Laure Guerit[1], Thomas Bernard[1,3], Mathilde Letard[4], Daniel Girardeau-Montaut[5], Vincent Godard[6], Rodolphe Cattin[7], Olivier Payrastre[8] and Philippe Steer[1]

[1]Univ Rennes, CNRS, Géosciences Rennes, UMR 6118, 35000, Rennes, France
[2]Univ Rennes, CNRS, Plateforme LiDAR topo-bathymétrique, OSERen, UAR 3343, 35000, Rennes, France
[3]Università di Trento, Italy
[4]Technical University of Munich, TUM School of Engineering and Design, Department of Aerospace and Geodesy, 80333, München, Germany
[5]CloudCompare
[6]Aix Marseille Univ, CNRS, IRD, INRAE, CEREGE, Aix-en-Provence, France
[7] Université de Montpellier, CNRS, Géosciences Montpellier, UMR 5243, , Montpellier, France
[8] Univ Gustave Eiffel, GERS-LEE, F-44344 Bouguenais, France

* correspondence: ron.nativ@univ-rennes.fr

https://doi.org/10.5194/egusphere-2026-724
Preprint. Discussion started: 31 March 2026

Abstract

We present a comprehensive workflow for processing a large-scale airborne Topo-Bathymetric LiDAR (TBL) dataset acquired over the 28 km Ardèche River Gorges in France during October 2021. To address limited depth penetration, low signal-to-noise ratio, and complex topography, we integrate onboard discrete returns, a full-waveform (FWF) re-analysis, and an orthorectified full-waveform synthesis (OrthoFWF). Depth penetration, evaluated by D_{99} (99^{th} percentile of retrieved water depth, D), increases from 2.88 m (discrete) to 3.70 m (FWF) and 4.48 m (OrthoFWF). Area coverage increases from 70.1% to 79.5% to 85.6% of the submerged area with bathymetric data available, while the length-based coverage (the percentage of river length composed of reaches with ≥95% bathymetric coverage) improves from 31.8% to 54.7% to 86.9%.A new unsupervised classification method, using a kernel-density–derived intensity threshold, was applied to 1.3 million points, enhancing the separation of bed returns from noise within the OrthoFWF domain and improving depth extraction. The workflow includes internal flight-line geometric correction, precision benchmarking against France's national LiDAR HD dataset, bathymetric classification with a random-forest classifier, and a targeted supplementary sonar survey to constrain the deepest reaches. To produce the final Digital Elevation Model from incomplete coverage, we compare three interpolation approaches and demonstrate that Poisson surface reconstruction yields the most morphologically realistic surfaces, particularly when constrained by sonar-derived depths. This integrated workflow substantially improves the accuracy and completeness of river bathymetry, supporting high-fidelity hydrodynamic modeling and advancing TBL applications in fluvial geomorphology.

https://doi.org/10.5194/egusphere-2026-724
Preprint. Discussion started: 31 March 2026

1. Introduction

Rivers are dynamic systems, shaped by the interplay between hydrodynamic forces and sediment transport, particularly during flood events (e.g., Leopold and Wolman, 1957; Baker 1977; Wolman and Miller, 1960). Understanding how these processes influence river morphology and vice versa is essential for aquatic ecosystems preservation, effective water resource management and predicting flood impacts in the context of a changing climate (e.g., Richards, 1982; Gordon et al. 2004; Meyer et al., 1999; Tsakiris and Loucks, 2023). However, the role of topography in shaping flood dynamics, and the resulting morphological changes driven by the interaction of flow and sediment transport, remains poorly understood across various spatial and temporal scales (Grant et al., 1990; Simpson and Schlunegger, 2003; cf. Tunnicliffe et al., 2024). This is especially relevant because many rivers are perennial (e.g., Van den Berg. 1995), and most 3D surface reconstructions may therefore fail to capture submerged features (Blais et al., 1993) that are critical for understanding channel morphology and hydrodynamic phenomena (e.g., Pike, 2002; Rezende et al., 2025).

Recent advances in technologies such as LiDAR, drones, and satellite imagery - coupled with increased computing power - have significantly improved our ability to acquire and process high-resolution Digital Elevation Models (DEMs)(e.g., Pike, 1988; Passalacqua et al., 2014; Tarolli, 2014). These tools have enabled detailed monitoring of topographic and morphological changes in river systems (e.g., Brasington et al., 2000), supporting the growing use of multi-temporal DEMs (e.g., Schwanghart and Scherler, 2014) and point clouds to track flood-induced landscape transformations (Lague et al., 2013; Yang et al., 2021). In particular, Topo-Bathymetric LiDAR (TBL) (Hickman and Hogg, 1969; Guenther et al., 2000; Wang and Philpot, 2007) has emerged as a powerful approach, combining high-resolution topographic data with bathymetric measurements to capture both above-water and submerged features in a single dataset (Quadros et al., 2008; Mandlburger et al., 2015; Lague and Feldman, 2020; Frizzle et al., 2024).

TBL sensors generally employ (i) a near infrared (1064 nm or 1550 nm) wavelength that captures reflected echoes from topographic entities such as ground, vegetation, and water surfaces, and (ii) a green (532 nm) wavelength that penetrates water bodies, enabling capture of the river bathymetry, along emerged topographic features (e.g., McKean et al, 2009; Tonina et al., 2019; Mandlburger et al., 2015; Fernandez-Diaz et al, 2014). The use of a green laser enables TBL

https://doi.org/10.5194/egusphere-2026-724
Preprint. Discussion started: 31 March 2026

overcoming the limitations of classical airborne LiDAR, which typically fails to retrieve information beneath water surfaces, thereby enabling more complete digitization of fluvial landscapes (e.g., Lague and Feldman, 2020).

While airborne TBL campaigns remain costly due to low operating altitudes and specialized sensors, recent advances in lightweight, unmanned aerial vehicles (UAV)-mounted topo-bathymetric LiDAR are improving accessibility for research and management applications (e.g., Mandlburger et al., 2020; Wang et al., 2022; Pfennigbauer et al., 2017; Islam et al., 2022). Nevertheless, TBL point-cloud processing is computationally intensive and further complicated by refraction correction and the classification of submerged returns, challenges that are particularly acute in steep, gravel-bed rivers with complex bedforms and spatially variable water surface elevation (Szafarczyk & Toś, 2022; Mandlburger et al., 2015; Letard et al., 2024; Guenther, 2000).

One major challenge lies in the limited depth penetration of the green (532 nm) laser, particularly in turbid or deeper waters. Fluvial environments tend to be more turbid than coastal environments (e.g., Lague and Feldmann, 2020), resulting in backscattered signals that are often too weak to image the deepest parts of the channel bed (e.g., Fernandez-Diaz et al., 2014). Two classical approaches exist to detect echoes: (i) onboard detection during the flight, producing herein termed "discrete" echoes and utilizing either the raw analog backscattered signal or a digitized version (Wagner et al., 2004; Fernandez-Diaz et al., 2014), or (ii) post-processing detection on the full-waveform (FWF) signal, which records the entire time-domain intensity signal (Guenther et al., 1988, 2000; Pan et al., 2015; Wang et al., 2015; Mader et al., 2023). FWF processing may reveal the presence of weak echoes that are not detected during the flight, either due to a penalizing signal-to-noise ratio or the close overlap of two echoes (Mallet and Bretar, 2009; Letard et al., 2021; Pan et al., 2015; Zhao et al., 2022; Mader et al., 2023). While this offers a promising avenue for recovering submerged terrain, it introduces further challenges, such as managing massive data volumes and distinguishing signal from noise (Stainbacher et al., 2021).

In some cases, complementary sonar surveys may be employed to fill acquisition gaps of submerged features (e.g., Coppo Frias et al., 2025), though these must be conducted in close temporal proximity to TBL acquisition and can be risky or logistically challenging, especially in dynamic, fast-flowing rivers. Interpolation techniques are also commonly used to estimate missing data, but the outcome is highly sensitive to both the chosen algorithm and the spatial variability of

https://doi.org/10.5194/egusphere-2026-724
Preprint. Discussion started: 31 March 2026

bed roughness. Despite recent advances in processing workflows (Mandlburger et al., 2015; Lague and Feldman, 2020; Frizzle et al., 2024) and classification methods (e.g., Letard et al., 2024), generating high-quality digital elevation models (DEMs), faithfully representing submerged riverbed geometries, remains an open challenge.

In this paper, we aim to illustrate the complete process of acquiring, processing, and preparing fluvial topo-bathymetric data from scratch, resulting in classified point clouds and workable DEMs. To illustrate this process chain in a complex environment, we use a novel Airborne TBL dataset from the Ardèche River Gorges in southern France, covering approximately 28 km of the river and collected during October 2021. The Ardèche River Gorges present substantial challenges in acquiring TBL data due to their unique geomorphic and hydrodynamic features. While the green laser beam used for bathymetry requires flying at 300 - 400 meters above ground level to maximize depth penetration (Lague and Feldman, 2020), these narrow and deeply incised gorges pose a risk to the sensor-carrying airplane, requiring a higher flying altitude and complicating its ability to achieve comprehensive survey coverage. Furthermore, alternating bedrock and sediment bed surfaces, along with small knickpoints and varying roughness, generate flow accelerations and white-water areas (e.g., Guenther, 1985; Philpot, 2019) that may backscatter the laser signal leading to minimal bathymetric capture. To maximize bathymetric coverage, it is therefore necessary to use the FWF characteristics, rather than relying solely on the onboard detected echoes.

We present a comprehensive dataset and complete workflow for planning and processing TBL in a complex, meandering bedrock canyon. We make five main contributions: (i) a new OrthoFWF plugin, called qFWF, in CloudCompare (Girardeau-Montaut, 2016) that generates orthorectified FWF layers for inspection and mapping; (ii) a novel unsupervised classification method that separates valid bathymetry from spurious returns in OrthoFWF data; (iii) a quantitative assessment of depth penetration and bathymetric coverage, comparing TBL processing strategies (discrete, FWF, and OrthoFWF detection) to quantify depth extension and the fraction of the channel bed retrieved; (iv) a rigorous evaluation of interpolation performance, contrasting Poisson Surface Reconstruction (PSR) (Kazhdan et al., 2006) with classical linear and kriging approaches to clarify their respective benefits and limitations where bathymetric data are missing; and (v) the delivery of analysis-ready final products, including cleaned topo-bathymetric point clouds and derived digital elevation models. We further assess the value of integrating independent sonar surveys where LiDAR optical penetration is limited, and justify seasonal survey timing to maximize

https://doi.org/10.5194/egusphere-2026-724
Preprint. Discussion started: 31 March 2026

coverage. Established components (e.g., 3DMASC) are included in the methods for completeness rather than presented as new results. All software, the complete workflow, and processed data products are released to support reproducibility and broader adoption in river-morphology applications.

https://doi.org/10.5194/egusphere-2026-724
Preprint. Discussion started: 31 March 2026

159

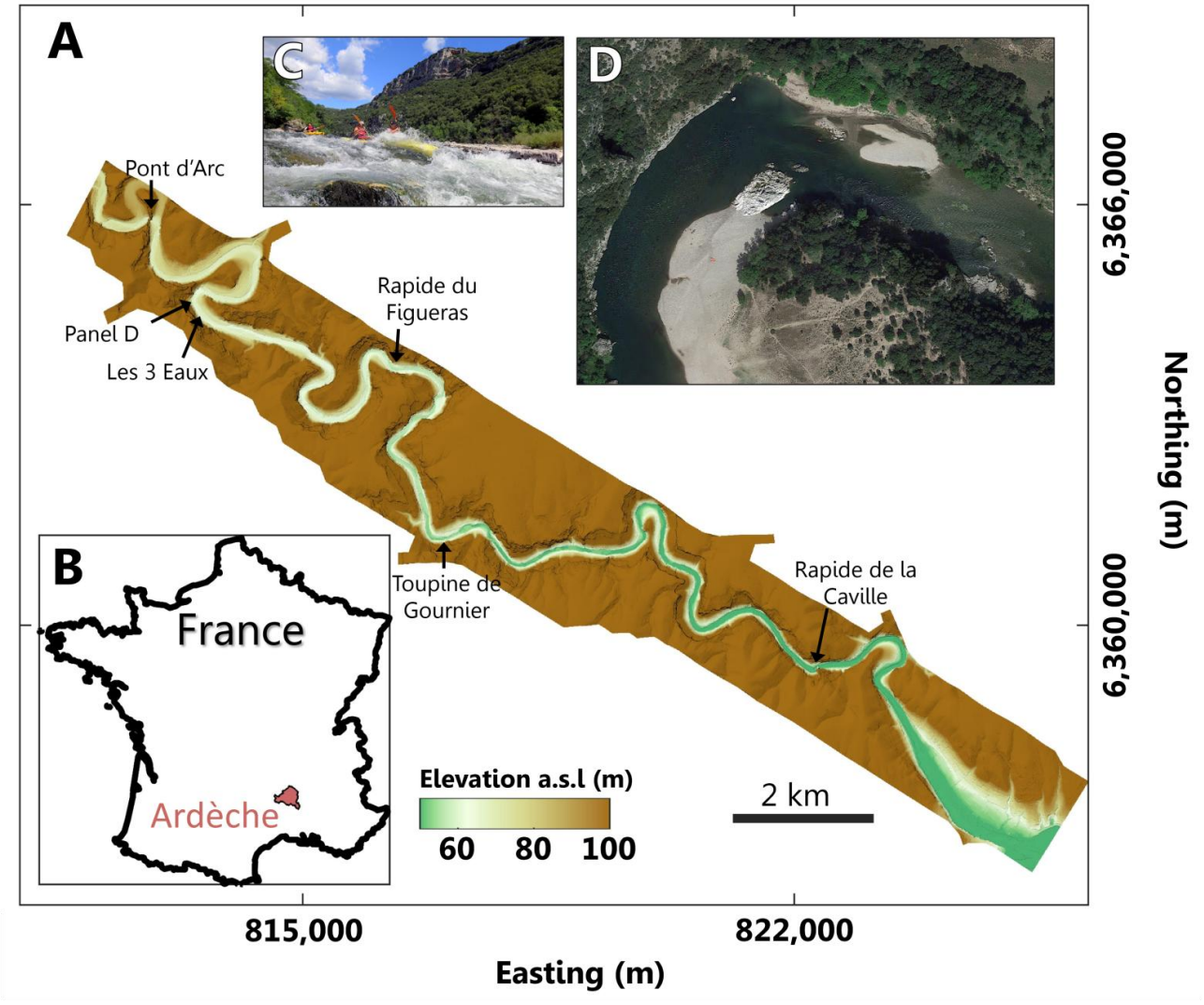

Figure 1: Overview of the field site in the Ardèche River. (A) 1 m DEM of the Ardèche Gorges, illustrating the river's relief and incised gorge. Common rapids and the Pont d'Arc are indicated in panels (B–D) (see also Figs. 8 and 10). (B) Location map showing the Ardèche catchment (highlighted in light red) within France. (C) a photo showcasing a typical rapid with white water in the Ardèche gorges. (D) Photograph of a typical gravel-bed bar in a sinuous reach of the Ardèche Gorges (reference location indicated in A; image sourced from © Google Earth). Coordinates are in meters and plotted using the RGF93 Lambert projection (EPSG:2154).

https://doi.org/10.5194/egusphere-2026-724
Preprint. Discussion started: 31 March 2026

2. Field Site: The Ardèche Gorges and survey setup

The Ardèche River, located in the mountainous Cévennes region of southern France, drains a catchment area of 2,370 km² and flows approximately 150 km from its headwaters at 1,600 m above sea level to its confluence with the Rhône River at 37 m above sea level (Fig. 1). The catchment is geologically diverse, with the upper basin dominated by metamorphic, granitic, and basaltic formations, while the lower reaches feature carbonate rocks. The Cévennes region is known for Mediterranean heavy-rainfall events (e.g., Le May and Saulnier, 2007), characterized by intense autumn storms that can last 1–2 days and may trigger catastrophic floods (Sheffer et al., 2003). These storms are driven by warm, moist air from the Mediterranean Sea, producing intense orographic rainfall during autumn. Total annual precipitation in the region ranges from ~1,000 to 1,100 mm. Regional hydrology is highly variable. Based on daily-mean discharge data from 1976 to 2025 at the Saint-Martin-d'Ardèche gauging station, the Ardèche River exhibits a mean annual discharge of 71 m³/s and an average annual peak discharge of approximately 1,100 m³/s. The lowest monthly discharges occur in July (≈12 m³/s on average), while the highest occur in November (≈139 m³/s). Over the 1976-2025 daily-mean discharge record, the maximum daily-mean discharge is 2,500 m³/s (2 December 2003; HydroPortail, station V5064010). Historical reconstructions indicate that the largest known floods in the late nineteenth century exceeded 7,000 m³/s in peak discharge (Lang et al., 2002).

In the downstream catchment, the Ardèche River flows through an approximately 30 km long bedrock gorge that records ~30 m of Late-Quaternary incision (Genuite et al., 2021). While the upstream Ardèche catchment is composed of crystalline rocks, the gorge is carved into carbonate rocks (Sheffer et al., 2003). The entire Ardèche Gorges is a natural reserve with a rich biodiversity. Quiet areas dedicated to birds of prey exist in various places with strict regulations for UAV and airborne activities during nesting periods that can extend to the end of September. The natural beauty of the gorge also attracts up to 2,000 kayaks on the river each day during summer vacations (July - August), which would significantly impact the quality of a TBL survey. As detailed in Lague and Feldmann (2020), a TBL survey should occur during (i) the lowest flow conditions possible, (ii) with the clearest water (i.e., never during or immediately after a flood), and ideally (iii) during leaf-off conditions to avoid green laser interception by the riparian vegetation on the river banks. Given the pluvial regime of the Ardèche watershed, this low-flow/leaf-off combination is never met. In winter, water levels are the highest and flying conditions are suboptimal. In early spring,

https://doi.org/10.5194/egusphere-2026-724
Preprint. Discussion started: 31 March 2026

water levels are usually very high. Without tourists and bird nesting constraints, an ideal acquisition time would be in August or early September during the lowest flows. Owing to the nesting period constraints, we chose to fly as early as possible in October. A narrow window of good weather allowed acquisition to take place on the 1st October 2021, with a mean daily discharge of 24 m^3/s. The lowest mean daily discharge in August-September 2021 was 6.7 m^3/s, highlighting that the acquisition did not occur at the lowest possible flow.

We used a dual wavelength (1064 nm and 532 nm) Titan DW instrument developed by Teledyne-Optech in 2014 (Fernandez et al., 2016) and operated since 2015 by the Universities of Nantes and Rennes in France. Details on the instrument can be found in Lague and Feldman (2020). The plane flew at 500 m above the lowest point of the gorge, at 170 km/h, with flight lines aligned along the main gorge and four cross-lines to increase geometrical robustness. The acquisition occurred early in the morning to avoid cloud formation. The total acquisition time, including turns, was 1h50. The Titan sensor uses an oscillating mirror creating a zig-zag pattern on the ground with a user defined maximum oscillating angle set to ±11°. The laser shot rate was set to 150 khz for each channel, with an overlap between flight lines of 25 %. The parameters were chosen to yield a mean shot density of 8 shots/m^2, for the 1,064 nm and 532 nm channels.

The resulting raw point clouds comprise a total of 1.641×10^9 points in the 1064 nm and 1.113×10^9 points in the 532 nm, compressed in LAZ format and resulting in ~13.1 GB in total. Higher point densities are possible, but we had to reduce the laser shot rate by a factor of two for eye safety constraints in the highest parts of the gorge. The Titan DW uses an onboard detection method to generate discrete echoes for each wavelength. An additional waveform recorder was attached to the sensor to record the FWF signal of each shot of the 532 nm channel. Control images were acquired by the Titan instrument but are not of sufficient resolution to generate a high quality ortho-image and were not used. Note that the 532 nm (resp. 1,064 nm) has a divergence of 0.7 mrad (resp. 0.35 mrad), which at 400 m corresponds to a laser spot size of ~28 cm (resp. ~14 cm).

3. Methods

In this section, we describe the key processing steps used to generate the final DEM. To help the reader visualize the available TBL information, Fig. 2 presents four LiDAR data products along a cross-section of the Ardèche River, displayed across three panels: (i) 1,064 nm discrete echoes and

https://doi.org/10.5194/egusphere-2026-724
Preprint. Discussion started: 31 March 2026

(ii) 532 nm discrete echoes (Fig. 2A), (iii) 532 nm FWF-derived echoes obtained with the manufacturer's software (Fig. 2B), and (iv) the raw 532 nm FWF signal itself (Fig. 2C). These cross-sections illustrate how wavelengths and detection modes provide complementary information: the near-infrared channel yields discrete returns primarily from topography and vegetation, whereas the green channel also penetrates the water column and returns bathymetry to a depth that depends on the echo-detection approach. The following subsections detail the processing of each data type and the characteristics of the underlying signals; Fig. 3 summarizes the end-to-end workflow from acquisition to DEM generation.

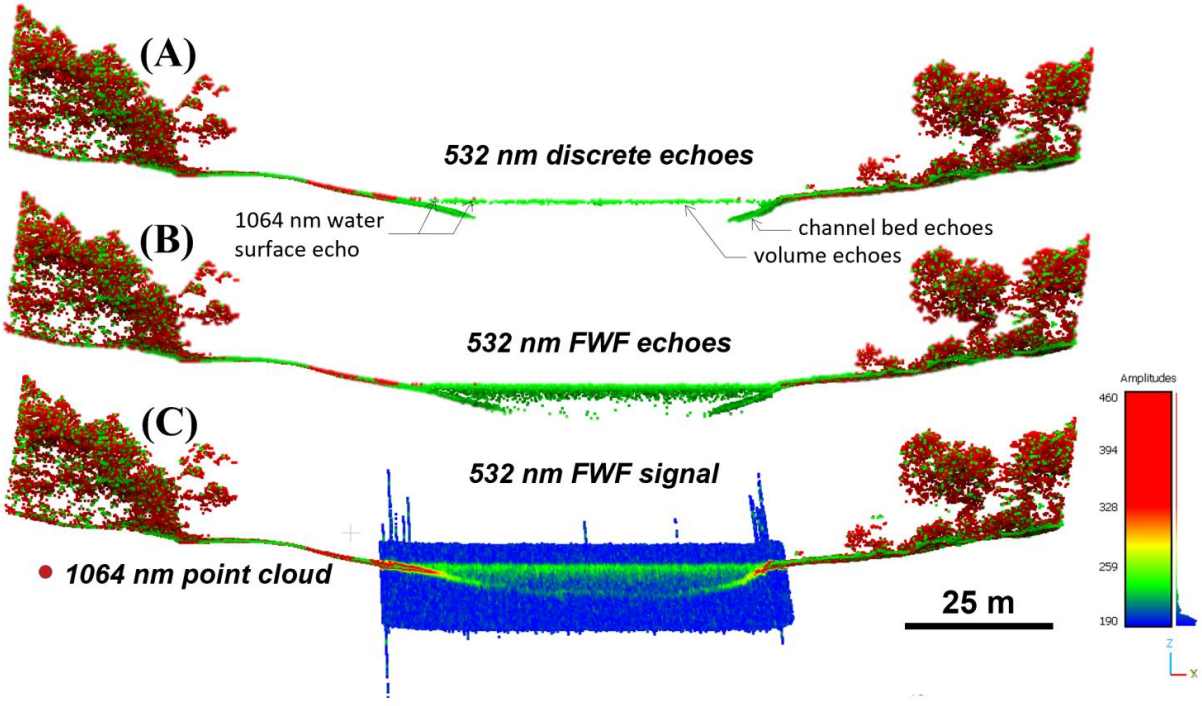

Fig. 2. Comparison of topo-bathymetric LiDAR outputs along a typical river cross-section. Red points denote 1064 nm returns from emergent terrain, and green points denote 532 nm discrete returns including submerged features. (A) Onboard discrete returns from both wavelengths, showing that the near-infrared channel does not penetrate water, whereas the green channel captures the channel bed but may miss deep-water echoes. (B) Post-processed discrete echoes extracted from the 532 nm full-waveform (FWF) data, revealing additional weak bottom returns absent from onboard recording. (C) Raw 532 nm FWF data, with intensity mapped from low (blue) to high (red); blue represents background signal, and green to red indicates the water surface, bed, and weak deep-bed echoes. FWF integration improves detection of overlapping or low signal-to-noise echoes. The visualization was generated in CloudCompare using the qFWF plugin.

https://doi.org/10.5194/egusphere-2026-724
Preprint. Discussion started: 31 March 2026

3.1 Generation and definition of discrete and full-waveform point clouds and georeferencing to the French national LiDAR survey

We produced two discrete-return point clouds corresponding to the 1,064 nm and 532 nm channels (Fig. 2A) using the manufacturer's proprietary software (Teledyne Optech, Laser Mapping Software LMS v4.4). These are hereafter termed PC_{1064} (near-infra red) and PC_{532} (green). The same software also re-detects echoes from the raw FWF record using a generic peak-detection algorithm, yielding a third point cloud that we denote PC_{FWF} (Fig. 2B). The point clouds are stored as standard *.laz* files, while the accompanying raw signal, FWF_{raw}, is stored in an external *.mdp* file (visualized in Fig. 2C). From FWF_{raw}, we additionally derived an orthorectified 1 m FWF (OrthoFWF; see Section 3.4.1 for definition) point cloud, $PC_{OrthoFWF}$, used for enhancing depth detection, quality control, and mapping (see Section 3.4.1). All three point clouds (PC_{1064}, PC_{532}, and PC_{FWF}) were then adjusted using BayesStripAlign v2.21 to refine the survey geometry. BayesStripAlign is a LiDAR strip-alignment and calibration tool that uses overlapping swaths to estimate geometric corrections automatically, including boresight, lever-arm, internal-geometry, and trajectory-related corrections. Here it was used to reduce vertical discrepancies between overlapping flight lines and to correct systematic inter-channel offsets between PC_{532} and PC_{1064} prior to classification and refraction correction.

The survey was then georeferenced to the LiDAR HD national French cover (https://geoservices.ign.fr/lidarhd), a benchmarked and freely available airborne topographic LiDAR dataset precisely georeferenced by the Institut National de l'Information Géographique et Forestière (IGN). For the Ardèche River Gorges, the available LiDAR HD survey occurred in March 2022. We refer to this point cloud as PC_{LHD}. We used roads and roofs to perform georeferencing of PC_{1064}, PC_{532} and PC_{FWF} using an Iterative Closest Point (ICP) processing, with respect to the PC_{LHD}. Following this, we used the M3C2 algorithm (Lague et al., 2013) to compute vertical distances between the PC_{532} and the PC_{LHD} point clouds. We used core points spaced by 1 m, a 2 m projection scale and filtered the results to keep only core points with a maximum distance uncertainty of 2 cm (Lague et al., 2013; Bernard et al., 2021). This last step allows us to automatically select core points located on horizontal, flat surfaces away from vegetation. These are represented by 6.72×10^5 points, mostly located on roads, parking areas, and flat roofs, all which are considered stable between surveys. The resulting distribution of M3C2 distances is

https://doi.org/10.5194/egusphere-2026-724
Preprint. Discussion started: 31 March 2026

261 approximately Gaussian (Fig. S1) with a mean and standard deviation of -0.51 ± 8.11 cm,
262 indicating a high level of vertical consistency.

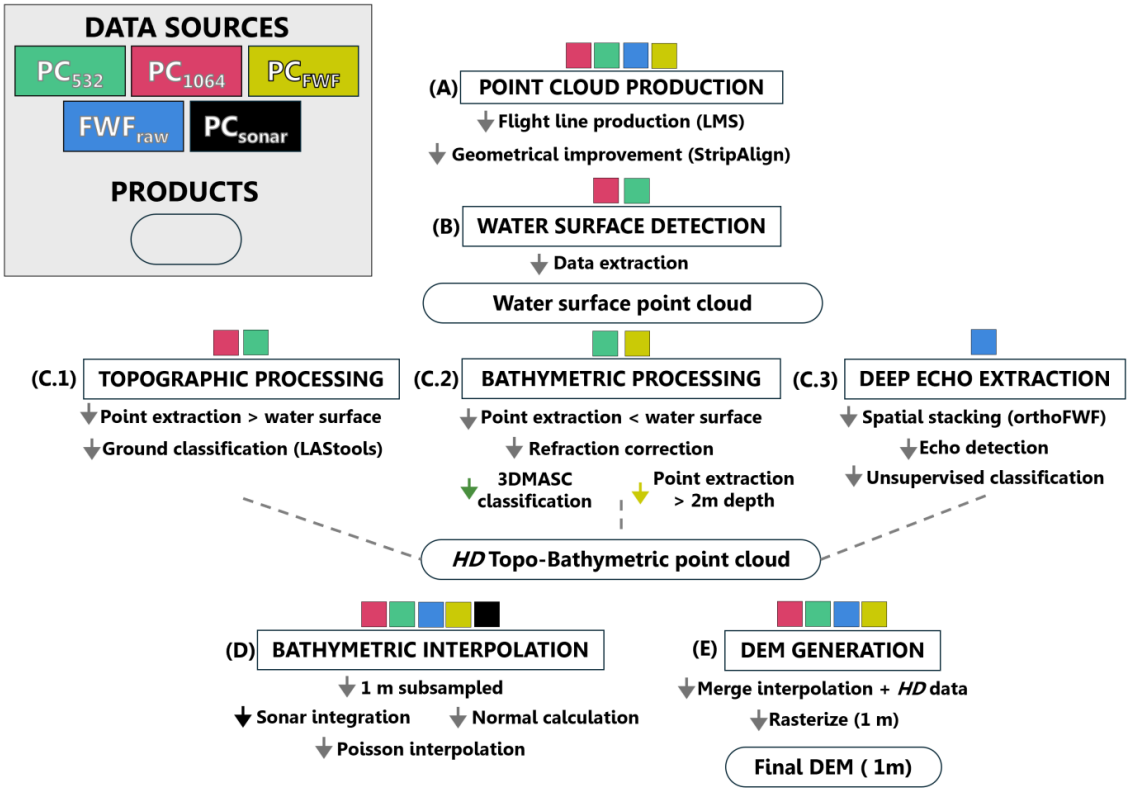

Fig 3. Workflow for DEM generation from multispectral discrete-return and full-waveform topo-bathymetric LiDAR. Point clouds are first derived from the 1064-nm and 532-nm channels (A), and a water surface is delineated from discrete echoes to separate bathymetric and emergent features (B). Processing then follows three branches: (C.1) topography extraction; (C.2) bathymetric processing from PC_{532} and PC_{FWF}; and (C.3) deep-echo extraction from $PC_{OrthoFWF}$ to extend depth and spatial coverage and reduce interpolation. Each branch includes specific classification steps. In (D), high-density products are thinned to a 1 m subsampled dataset, and sonar measurements are added only to guide bathymetric interpolation, not to build the final DEM. The final DEM uses interpolated points only where high-density data are absent. Vertical arrows indicate intermediate steps. Colors: red = PC_{1064}, green = PC_{532}, yellow-green = PC_{FWF}, blue = $PC_{OrthoFWF}$, black = sonar. See Sect. 3.1 for data definitions.

263

264

https://doi.org/10.5194/egusphere-2026-724
Preprint. Discussion started: 31 March 2026

3.2 Water surface detection and ground classification

Water surface detection primarily relies on echoes from the 1064 nm channel, which reflects upon contact with the water surface. In contrast, returns from the 532 nm channel often include subsurface *volume echoes*, that typically lie between 0 and 0.7 m below the actual water surface (Figs. 2 and 3), complicating their use for precise water surface delineation (Guenther et al., 1988, 2000; Höfle et al., 2009; Mandlburger et al., 2013; Pan et al., 2015; Lague and Feldmann, 2020). Accurate identification of the water surface is essential, as it underpins key processing steps such as bathymetric points extraction and refraction correction, but is also a key hydrological information that can be used for instance for flow resistance calculations (e.g., Lague and Feldmann, 2020).

Challenges are numerous for water surface detection of large-scale topo-bathymetric surveys (e.g., Lague and Feldmann, 2020). While the Ardèche River Gorges are mostly a single water body without significant dams, infrastructure and connected water bodies, the lack of wind on the day of the survey made the low velocity flow zones appearing like mirror surfaces for the laser resulting in numerous specular reflections that do not create an echo in the 1,064 nm channel. This made the detection of the water surface more complex than in other surveys, such as the Ain River (Lague and Feldmann, 2020). Instead of employing a machine learning approach (e.g., Letard et al., 2024, Shaker et al., 2019), which requires training, we utilize an algorithm based on geometric operations and filtering, implemented through command-line tools in CloudCompare. To detect the water surface, the algorithm leverages the similarity between the 1064 nm and 532 nm point clouds over hard, opaque surfaces (e.g., ground and buildings), while accounting for their differences over water bodies, where the 532 nm wavelength penetrates the surface, and in vegetated areas, where differing incident angles and footprints result in distinct sampling of tree structures for each wavelength (fig. 2A) (Letard et al., 2024). Yet, the water surface sampled by the 1,064 nm is a planar, low slope surface, whereas trees are never planar. This helps in separating the two types of zones where the 1,064 and 532 nm waveforms differ.

The algorithm begins by thinning PC_{532} and PC_{1064} to a 1 m resolution, retaining the lowest point within each 1 m² pixel. This operation removes a large portion, though not necessarily all, of the vegetation and enables processing of the entire survey area at low resolution in a single step. Note that the submerged areas of the PC_{532} now represent either the channel bed or a volume echo if the

https://doi.org/10.5194/egusphere-2026-724
Preprint. Discussion started: 31 March 2026

river was locally too deep, as would be the case in fig. 2A. We then compute for PC_{1064} three attributes: (i) the vertical distance to the nearest PC_{532} point, and within a 5 m spherical neighborhood (ii) the local slope and (iii) the number of points. A first set of seeds of the water surface is created from points at least 10 cm above PC_{532}, with a local slope of less than 1° and with at least 5 neighbors. Finally, the algorithm iteratively propagates the water surface laterally from the seeds by including further PC_{1064} thinned points that are (i) within 10 m of existing surface points, (ii) above the PC_{532} and (3) do not deviate more than 1° from the existing surface points. The final result is manually validated to ensure that the 1 m resolution water surface point cloud is error-free, yielding the reference water surface point cloud PC_{ws}.

We then split PC_{532}, PC_{1064} and PC_{FWF} based on the sign of the vertical offset relative to the nearest PC_{ws} water-surface point ($\Delta z = z - z_{ws}$), yielding a topographic (above-water; $\Delta z > 0$) point cloud for both channels and a bathymetric (below-water; $\Delta z < 0$) point cloud for the 532 nm channel (Fig. 3). We use LAStools to extract ground data for the 532 nm and 1,064 nm topographic point clouds (Hug et al., 2004), with the *lasground_new* command adequate for natural terrain and high precision (*nature* and *extra_fine* parameters). This applies geometric filtering and progressive Triangulated Irregular Network densification to distinguish ground from vegetation and other non-ground objects. The resulting ground point clouds in the 532 and 1,064 nm channels form the topographic component of the full topo-bathymetric dataset (Fig. 3).

3.3 Bathymetric Processing

3.3.1 Refraction correction

As the 532 nm laser pulse penetrates the water surface, it is refracted according to the classical law of refraction (often referred to as Snell's law) and its velocity decreases by a factor $1/n$, where n is the refractive index of water. Because the processing assumes light travels in air, underwater returns are initially placed at incorrect positions unless refraction and water-velocity corrections are applied. As a result, points appear significantly deeper than they are (by 26 - 29% for the Titan scanning pattern) and can be displaced by up to 1 m horizontally at 5 m depth (Lague and Feldmann, 2020), emphasizing the importance of refraction correction. The manufacturer software does not provide a convenient solution to process a complex river with varying water surface elevation, and we thus recompute the refraction correction. We assume a locally horizontal water surface which is an acceptable assumption for fluvial environments given the very low river slopes,

https://doi.org/10.5194/egusphere-2026-724
Preprint. Discussion started: 31 March 2026

the small amplitude of surface waves, and the limited water depth. Only in rapids with a surface slope of a few degrees could this hypothesis be incorrect. However, because of the typical very low flow depth (< 1 m) in rapids, the uncertainty introduced by this assumption remains smaller than a few cm vertically and horizontally.

We first compute the 3D laser shot vector using the aircraft trajectory and the point position, then estimate the local apparent water depth by using the nearest water surface point in PC_{ws}. An (X, Y, Z) geometric correction is applied to each of the bathymetric PC_{532}. We assume a refractive index of n = 1.333, corresponding to freshwater at 20 °C. This refraction correction is applied to all submerged points in the PC_{532} and PC_{FWF} datasets. The correction is performed using command-line operations in CloudCompare and Python, and is computationally efficient, typically completed in under a few minutes.

3.3.2 Channel bed classification of shallow echoes

In clear water conditions, the backscattered green laser energy typically produces two distinct echoes in shallow aquatic environments (Fig. 2A): a *volume echo*, occurring between 0 and 1 m below the water surface and influenced by water surface and column properties (Guenther et al., 1988, 2000; Höfle et al., 2009; Mandlburger et al., 2013; Pan et al., 2015; Lague and Feldmann, 2020), and a *bathymetric echo*, which corresponds to the riverbed. While the volume echo is systematic, the bathymetric echo only exists if enough energy is backscattered from the bed. When the bathymetric echo is systematic, i.e., when the channel bed is fully covered, classifying these points is straightforward, as the bathymetric return typically corresponds to the last echo, aside from occasional noise. In the case of the Ardèche, the bathymetric cover is only partial with the PC_{532} and PC_{FWF}. All submerged points should thus be classified as volume echoes or true riverbed. Over a 28 km long survey with a complex bathymetry, this cannot be done manually. We therefore used 3DMASC (3D classification using Multiple Attributes, Scales, and Clouds; Letard et al., 2024), an explainable machine-learning workflow for 3D point-cloud classification. Developed for dual-wavelength topo-bathymetric LiDAR data, it combines multiscale geometric descriptors and backscatter-intensity features from multiple point clouds to classify points into relevant surface classes. Although 3DMASC has achieved high accuracy (> 0.95) in similar bathymetric classification tasks, it may require retraining for different bathymetric environments (Letard et al., 2024).

https://doi.org/10.5194/egusphere-2026-724
Preprint. Discussion started: 31 March 2026

355

356 In the 3DMASC classifier, training and validation datasets are generated following the
357 methodology outlined by Letard et al. (2024). This involves identifying representative cross-
358 sections along the gorge and manually labelling two classes in PC532: water-column (volume)
359 echoes and bathymetric echoes. We choose a mix of cross-sections with clear visual separation of
360 bathymetric points and water-column points, and cases with only water-column points. Additional
361 challenging cases included: (i) shallow water zones, with typical depths smaller than 50 cm, where
362 the proximity of bathymetric and volume echoes makes the separation difficult; and (ii) cross-
363 sections with significant tree interception and/or complex bedrock bank geometry that results in
364 sparse sampling of the bed or complex underwater bank geometry. These samples were split into
365 a training dataset with 4,000 samples per class (8,000 total) and a validation dataset sampled in
366 different locations than the training cross-sections.

367 Three point clouds are used to compute 3DMASC features: PC_{532}, PC_{1064} and PC_{ws}. The latter is
368 used as a context point cloud to retrieve the vertical distance of each point to the water surface
369 using *k*-nearest neighbors, with *k* ranging from 1 to 4 (see Letard et al., 2024). We use an initial
370 set of features containing multi-scale geometry and intensity characteristics computed over
371 spherical neighborhoods with the following set of diameters: 1.5, 2.5, 4, 6 and 8 m. We do not
372 perform classifier tuning as possible with the advanced 3DMASC tools. The classifier achieves an
373 overall accuracy of 0.95 (evaluated on the validation dataset), with balanced performance across
374 classes and F1-scores around 0.95 (Table S1). Figure 4 shows a typical example of classification
375 results and the classification confidence, ranging from 0 to 1, as predicted by 3DMASC.

376 To obtain a complete and reliable bathymetric dataset, we first perform an initial 3DMASC
377 classification and then manually validate the results in CloudCompare. Misclassified bathymetric
378 points are reclassified as volume echoes along the entire gorge, leaving a cleaned dataset
379 representing the true bed. To assist future users of 3DMASC in selecting suitable features for
380 bathymetric-point classification, we conduct an additional analysis to identify a more minimal and
381 effective feature set. This analysis uses the cleaned, gorge-wide dataset to capture a broader range
382 of bathymetric conditions than the initial training sections. Because these results are not central to
383 the main objectives of this study, but may be of interest to 3DMASC users, we present them in the

https://doi.org/10.5194/egusphere-2026-724
Preprint. Discussion started: 31 March 2026

Supplementary Material (Table S3). We then proceed with the bathymetric extraction from the FWF dataset.

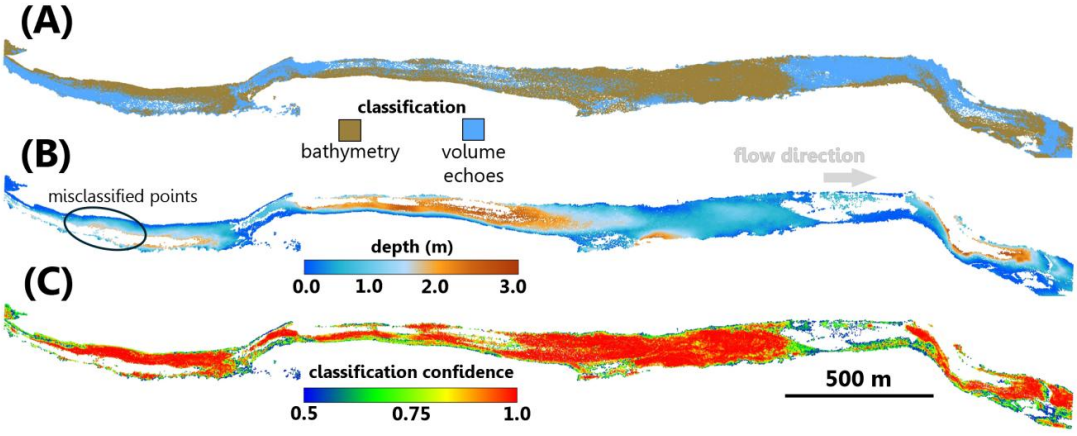

Fig. 4: Initial bathymetry classification using 3DMASC in a typical 2 km long river reach with incomplete channel bed coverage. (A) color-coded by classification: blue = volume echoes, brown = channel bed. (B) Water depth after volume echoes have been removed; this layer can be used to identify potentially misclassified points. (C) Classification confidence values generated by the 3DMASC algorithm, ranging from 0.5 to 1, which are used to identify low-certainty points.

3.4. Deep echo extraction from FWF data

Post-flight detection of echoes in the FWF data enables deeper signal penetration, owing to a lower signal-to-noise ratio threshold compared to onboard discrete echo detection (Figs. 2B). However, this approach alone does not provide a full bathymetric coverage in the case of the Ardèche River Gorges. Here, we aim to further extend the maximum detectable depth by enhancing the signal-to-noise ratio through spatial stacking of the FWF signal (Fig. 5).

A similar approach has been used in previous work, albeit on much shorter river reaches of a few km (Mader et al. 2019, 2021, 2023b; Pan et a., 2016) or in simpler coastal environments (e.g., Launeau et al., 2019; Mader et al., 2023a). Here, a significant challenge lies in processing 28 km of rivers in an automated way.

https://doi.org/10.5194/egusphere-2026-724
Preprint. Discussion started: 31 March 2026

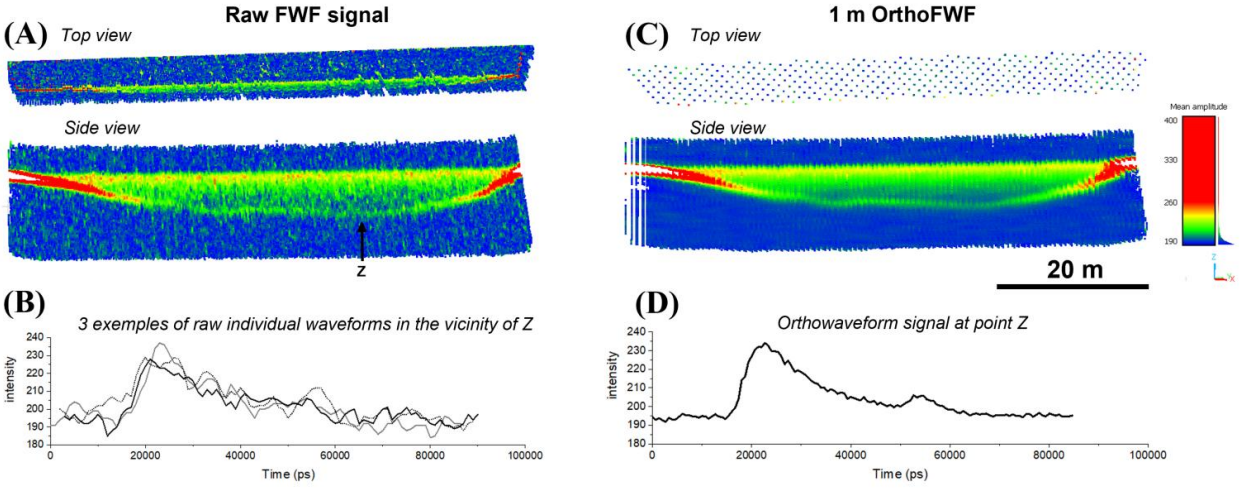

Fig. 5. Comparison of the raw FWF signal and the reprojected, stacked OrthoFWF signal along the same cross-section as in Fig. 2. (A) Raw FWF samples converted to a point cloud and colored by intensity using the qFWF plugin in CloudCompare. (B) Three raw waveforms near point Z, showing the difficulty of identifying the bottom echo under low signal-to-noise conditions. (C) Reprojected and stacked OrthoFWF signal; the top view shows the 1 m horizontal spacing over the same extent as in panel A, and the side view shows the channel bed more clearly after noise reduction. (D) Reprojected OrthoFWF signal near point Z, where the bottom echo becomes detectable after stacking and is used to extract OrthoFWF echoes.

3.4.1 OrthoFWF generation

We develop an open-source plugin (qFWF; Lague et al., 2025), freely available in CloudCompare, that generates orthowaveforms (OrthoFWF) and allows simple echo detection. This complements the CloudCompare's ability to open and visualize the FWF signal, a functionality added by our team and the creator of CloudCompare in 2018. We aim to generate OrthoFWF, which are gridded 3D representations of FWF LiDAR signals, including spatial averaging (Yao and Stilla, 2010; Magruder et al., 2010; Pan et al., 2016; Mader et al., 2019, 2021, 2023b). Unlike raw waveform data, which are tied to individual, irregularly distributed laser shots (Fig. 5A), OrthoFWF reorganizes the information into a regular raster grid, similar to orthophotos (Fig. 5B). Each pixel of size *dx* in the OrthoFWF grid stores the vertical distribution of backscattered energy for that spatial location (i.e., the waveform) at a vertical sampling *dz* identical for all waveforms. This format facilitates direct comparison and fusion with other raster-based datasets, such as hyperspectral imagery (Pan et al., 2016), or to improve the signal-to-noise ratio for weak echo detection in deep water or shallow turbid water (Launeau et al., 2019; Mader et al., 2019, 2021,

https://doi.org/10.5194/egusphere-2026-724
Preprint. Discussion started: 31 March 2026

2023). In our approach, we turn all samples of the bathymetric waveforms into 3D points with their associated signal intensities (as in Fig. 2A and 5A) and then work on voxelizing this 3D point cloud on a grid of horizontal (resp. vertical) spacing *dx* (resp. *dz*). Unlike other approaches, the signal assigned to the center of each voxel is averaged within a cylindrical volume of thickness *dz* and radius *r*, where *r* exceeds the horizontal spacing *dx*. This allows for horizontal stacking of the signal over distances larger than the final OrthoFWF resolution. While this results in oversampling, it significantly improves the signal-to-noise ratio and can enhance the detection of very weak echoes over flat, horizontal beds. Figure 5 presents examples of OrthoFWF grids and both raw and stacked waveforms, illustrating the signal-to-noise improvement in the case of the Ardèche River Gorges.

Given that the waveforms are sampled every 1 nanosecond for this sensor, corresponding to approximately 15 cm in air and 11 cm in water, and that we expect at least 8 shots/m², we choose to generate OrthoFWF using dx = 1 m, dz = 0.1 m and r = 2 m. Note that we did not correct the waveforms for refraction and celerity as in Mader et al. (2023), as we have not yet implemented this option in CloudCompare. We justify this simplification below. The Titan's 532 nm channel typically has incidence angles on the water surface varying between a minimum of 10° and 17°, resulting from a combination of 7° of 532 nm laser forward pitch, 3° of forward plane pitch and 0° to 11° of scan angle perpendicular to the plane direction. At these angles, the true depth of a FWF sample is at a rather constant factor of 0.73 of the apparent depth before refraction correction. Hence, not accounting for refraction does not significantly alter the vertical distribution of intensity across shots within the same water volume. However, the refraction of the shots induces a horizontal uncertainty that increases with depth, reaching 60 cm at 4 m depth for an incidence angle of 15°. Nevertheless, the 2 m averaging radius and the 1 m discretization of the orthoFWF limit the impact of this error. We thus only apply a correction to the apparent depth of the orthoFWF detected echoes of a factor of 0.73, all this being done in CloudCompare.

Once the OrthoFWF are generated (Fig. 5D), peaks must be detected to create a point cloud. Advanced processing methods can be used to extract echoes with or without a dedicated physical model to separate the various components of a bathymetric return (Abady et al., 2014; Wang et al., 2015; Mader et al., 2023a). They may be relatively complex and have not yet been implemented in the CloudCompare plugin. In contrast, our approach is deliberately more straightforward: we

https://doi.org/10.5194/egusphere-2026-724
Preprint. Discussion started: 31 March 2026

apply a basic local maxima algorithm designed to detect even the faintest peaks above a manually defined threshold. This method prioritizes sensitivity over selectivity, and as a result, introduces significant noise. The main challenge then becomes identifying the true bed surface among such noise, as detailed in Section 3.4.2.

We note that, unlike methods that fit echo positions using specific functions (e.g., Gaussian fitting), the local maxima algorithm yields a vertical resolution equal to the waveform's sampling interval. Consequently, after refraction correction, the OrthoFWF echo positions are known with a vertical resolution of 7.3 cm.

From the raw PC_{FWF}, we extract returns at depths > 2 m (Fig. 3).

3.4.2 Unsupervised noise filtering for deep OrthoFWF classification

We develop an unsupervised filtering procedure that performs the deep OrthoFWF bed versus noise classification by exploiting the statistical distribution of echoes in the intensity-water depth space. Because shallow bathymetric points are far more numerous, we analyze points within 2.5 - 4.5 m depth and compute a two-dimensional kernel density estimate (KDE) over a regular grid in depth and $\log_{10}$(intensity). The dataset comprises ~1.32 million echoes that include a mixture of real bed signals and noise. At 532 nm, for a given depth we assume higher intensities correspond to real bathymetry, whereas lower intensities correspond to spurious “peaked” local minima in the raw FWF returns. Under this assumption, more reliable (bed) and less reliable (noise) echoes should concentrate in distinct regions of the intensity-depth plane; the 2D KDE makes these modes explicit and enables a data-driven separation boundary between them, which we then use for classification and for estimating the attenuation parameters.

3.5 Continuous topo-bathymetric DEM generation

Here we outline the final steps for generating a 1m grid size DEM through interpolation when bathymetric data is missing and the interest of using low-quality sonar data to improve the DEM quality in the deepest part of the gorge where even OrthoFWF echoes are missing. We also use the opportunity provided by the OrthoFWF deep echoes to evaluate the quality of interpolation methods that would only be based on a reduced penetration depth, i.e., with only discrete echoes.

https://doi.org/10.5194/egusphere-2026-724
Preprint. Discussion started: 31 March 2026

3.5.1 Comparison of interpolation methods for fluvial TBL

To complete the DEM generation, we evaluate the accuracy of various interpolation techniques available in CloudCompare, by leveraging the $PC_{OrthoFWF}$ as an independent reference surface of the deepest part. Our objective is to identify the most suitable method for reconstructing continuous bathymetric surfaces from incomplete datasets. We compared three interpolation methods: (i) linear, (ii) kriging, and (iii) Poisson Surface Reconstruction (PSR), each evaluated against the $PC_{OrthoFWF}$.

Linear interpolation estimates unknown values by assuming the surface varies linearly between neighboring observations (i.e., a locally planar approximation). It is computationally efficient and can preserve sharp breaks, but may produce overly flat artifacts where data gaps are large or terrain is complex.

Kriging is a geostatistical method that predicts unknown values using spatial autocorrelation and a modeled covariance structure. Weights are computed from the covariance model for surrounding points, allowing statistically robust surface predictions, especially in datasets with moderate density and known spatial structure (e.g., Heritage et al., 2009; Merwade et al., 2008). This type of interpolation is supported by the rasterize function in CloudCompare.

Poisson Surface Reconstruction (PSR) creates a continuous surface by solving a spatial Poisson equation over an oriented point cloud, using the input normals and point positions to produce a smooth, watertight surface that fills gaps in a geometrically consistent way (Kazhdan et al., 2006). PSR is particularly suited for reconstructing natural surfaces with gradual transitions and limited sharp discontinuities. In this study, PSR was applied directly in CloudCompare. The method first computes surface normals using a user-defined scale, then generates a mesh. We focus on two main parameters influencing the reconstructed surface: the normal radius scale and the Poisson reconstruction resolution. In each case, one parameter was kept constant while the other was systematically varied. To evaluate the PSR sensitivity to these parameters, we compare the reconstructed surfaces with the reference $PC_{OrthoFWF}$. Vertical distances are computed as mesh-to-cloud distances, and parameter performance is quantified using the mean and standard deviation of the resulting error distributions.

The PC_{532} point cloud is first subsampled to 0.5 m as minimum distance between points. For the PSR, we vary the neighborhood radius used for normal estimation (1, 3, 5, and 10 m) and the

https://doi.org/10.5194/egusphere-2026-724
Preprint. Discussion started: 31 March 2026

reconstruction resolution (1, 3, 5, 10, and 15 m). Vertical distances are computed as cloud-to-cloud differences for linear and kriging, and as mesh-to-cloud distances for PSR. To ensure a consistent comparison domain, all point clouds are clipped to the Ardèche River Gorges extent. In addition, isolated PC_{FWF} returns are removed using connected-component filtering to exclude spatially disconnected points that are likely noise and can introduce local interpolation artifacts and bias error statistics. Each method is applied to the full dataset using only PC_{532} and differences are computed only at locations where $PC_{OrthoFWF}$ data are available. We report the mean and standard deviation of these differences, based on more than 200,000 points per parameter set.

3.5.2 Sonar survey to enhance bathymetric coverage

While the TBL survey provides high-resolution bathymetric data, it is unable to penetrate deeper water zones that characterize the Ardèche River Gorges, along narrow incised bedrock reaches, and in the outer bends of meanders. When only a small portion of the riverbed is missing, complementary sonar data are not essential, as interpolation can adequately fill the gaps. However, when a larger fraction of the channel bed is missing, additional sonar data can support and improve the interpolation process. Due to logistical constraints, we conducted the sonar survey approximately 3.5 years after the original LiDAR acquisition. In a dynamic river gorge such as the Ardèche, this time gap inevitably leads to changes in the channel bed, on the order of several tens of centimeters. Nevertheless, in areas where LiDAR bathymetric coverage is extremely limited, such as the narrowest sections of the gorge, sonar measurements, even with their inherent uncertainties, are preferable to having no data at all. They provide crucial information, such as whether the deepest part of the channel is at 5 m or 10 m depth.

A kayak-based sonar survey was carried out on May 28–29, 2024, covering a ~25 km reach of the Ardèche River between Pont d'Arc (44.381642°, 4.414472°) and Saint-Martin-d'Ardèche (44.309437°, 4.553543°). The system used was a Deeper Chirp+ sonar unit (https://deepersonar.com), mounted at the stern of a kayak, sampling the channel bed at 1 Hz, with a stated depth precision of 1 cm, resulting in a typical point spacing along the kayak track varying between 1 and 2 m depending on the kayak velocity. Areas with missing LiDAR bathymetry were specifically surveyed with a higher number of cross sections and ensuring also an overlap with LiDAR covered bathymetry. Data acquisition by the sensor includes water depth, and geographic position (latitude, longitude), estimated using a smartphone connected by WIFI to the sensor. The

https://doi.org/10.5194/egusphere-2026-724
Preprint. Discussion started: 31 March 2026

GNSS horizontal position uncertainty of the smartphone is expected to be around 0.5 m (1 standard deviation). Yet, given the reduced sky visibility in the gorge, the variable lever-arm between the smartphone and the sensor related to the kayak orientation, we conservatively assume that the horizontal uncertainty of the depth sounding is 1 m (1 standard deviation).

As the vertical positioning of the smartphone is at best 1 or 2 m and is not useful, we use a two-step approach to generate a sonar bathymetric point cloud to be used with the LIDAR data: first, depth values are converted into a *relative* sonar PC by assuming that the sensor elevation is the water surface elevation from the PC_{1064}. Because discharge during the sonar survey was ~33 m^3/s (vs. ~24 m^3/s during LiDAR acquisition), the water surface was likely higher during the sonar survey. Using the LiDAR-derived water-surface elevation to reference sonar depths therefore likely biases the sonar-derived bed elevations upward relative to the LiDAR-referenced bed. To correct for this offset, we compare the sonar PC to the 2021 discrete LiDAR channel bed echoes by using a vertical M3C2 distance measurement with a projection scale of 1 m. This comparison results in a median difference of 46.2 cm ± 63.1 cm. We thus shift the relative PC vertically. We use the standard deviation of 63.1 cm as a measure of the vertical uncertainty of the sonar data. Additionally, the sonar data is used only where no bathymetric LiDAR information is available.

3.5.3 Creation of the final DEM product and evaluation of survey performance

The final 1 m-resolution DEM is generated in CloudCompare following the workflow shown in Fig. 3. Note that the sonar point cloud itself is not directly inserted into the final DEM; it serves only to guide surface reconstruction via Poisson Surface Reconstruction (PSR). First, the raw LiDAR point clouds (PC_{532}, PC_{1064}, PC_{FWF}, and $PC_{OrthoFWF}$) are filtered to remove erroneous/outlier points (hereafter referred to as the *cleaned* point clouds) and then merged and spatially subsampled to 1 m. The sonar-corrected bathymetry is then merged with this subsampled LiDAR dataset. Next, surface normals are computed using a neighborhood radius of 3 m to enable surface reconstruction, and PSR is then run with a user-defined resolution of 3 m to produce a continuous mesh. A justification for these parameter choices is provided in Section 4.3. The mesh is resampled to a point cloud at 2 pts m^{-2}. Interpolated points for areas lacking LiDAR coverage are assigned a unique class and merged back with the *HD* data (original PC_{532}, PC_{1064}, PC_{FWF}, and $PC_{OrthoFWF}$). Finally, we rasterize the dataset to a 1 m DEM; because only a very small fraction of

https://doi.org/10.5194/egusphere-2026-724
Preprint. Discussion started: 31 March 2026

pixels remains without data (e.g., beneath vegetation), we apply a linear interpolation to fill those gaps.

Bed elevation and water-surface variables are first derived from the gridded TBL products. Bed elevation is sampled along the flow path using a steepest-descent algorithm computed on the 1 m DEM in TopoToolBox (Schwanghart and Scherler, 2014), yielding a raster-based centerline sampled at ~1 m spacing (with minor step-length variability due to routing). A corresponding low water-surface profile is extracted from the LiDAR-derived water-surface grid by taking, at each stream node, the 2nd percentile of water-surface elevation within a 100 × 100 m window centered on the node and restricted to the mapped wetted area.

We evaluate overall TBL survey performance using bathymetric observation coverage (data support) metrics rather than the completeness of the interpolated DEM. Bathymetric coverage performance is quantified using two metrics: (i) overall coverage, defined as the fraction of wetted pixels containing at least one bathymetric return, and (ii) length-weighted coverage at a 95% threshold, defined as the proportion of river length for which individual cross-sections achieve at least 95% coverage, a level at which interpolation is negligible. These metrics are computed for three processing data complexity levels: (1) discrete onboard echoes ($PC_{532} + PC_{1064}$), (2) discrete plus full-waveform echoes ($PC_{532} + PC_{1064} + PC_{FWF}$), and (3) the whole dataset ($PC_{532} + PC_{1064} + PC_{FWF} + PC_{OrthoFWF}$).

Coverage at each stream node is defined as the fraction of DEM grid cells within the wetted mask inside a 50 × 50 m window that contain at least one LiDAR bathymetric return (i.e., a point classified as submerged bed) in the underlying point cloud for the corresponding processing level. The computation is constrained by a polygonal water mask digitized in qGIS from the PCWS. Water-depth statistics are computed within the same moving windows as the difference between the LiDAR-derived water-surface grid and the bed DEM, reporting the mean, $\pm 1\sigma$, and the 99th-percentile depth. All metrics are referenced to downstream distance from the headwaters to the outlet, with selected gorge rapids identified for context.

https://doi.org/10.5194/egusphere-2026-724
Preprint. Discussion started: 31 March 2026

4. Results

4.1. Unsupervised $PC_{OrthoFWF}$ noise filtering

Figure 6A shows the result of the KDE and the unsupervised classification of bed echoes and noise in the $PC_{OrthoFWF}$ data. We identify two distinct clusters in the intensity-depth space: the upper (high intensity) corresponds to channel-bed echoes, and the lower (low intensity) to noise, for similar depths. Consistent with expected signal attenuation and prior observations (e.g., Lague and Feldmann, 2020), channel-bed intensity, I_b, displays a clear exponential decay with water depth, D:

$$I_b = I_{ref} e^{-2K_{d,532} D} \quad (1)$$

where I_{ref} is a coefficient and $K_{d,532}$ is the attenuation coefficient for the 532 nm channel. Using the KDE-maximum ridge, the exponential fit over depths of 2.6 - 4.0 m yields $I_{ref} = 351$ and $K_{d,532} = 0.4430 \pm 0.0066$ (standard error; SE) ($R^2 = 0.97$).

The separation between noise and bed echoes follows an exponential decay defined by the local minima of the KDE at each depth (Fig. 6A). We use this observation to define a conservative separation boundary by fitting an exponential model to these minima and offsetting it upward by 10% in intensity. This buffer intentionally favors precision over recall: it reduces the likelihood that water-column noise is misclassified as bed, at the expense of potentially excluding a small fraction of low-intensity bed echoes near the detection limit. This conservative boundary still cleanly isolates the bed-echo population across depths, indicating that the method reliably separates bed returns from water-column noise (Fig. 6B,C). The $PC_{OrthoFWF}$ thus significantly extends the measurable depth range (e.g., D_{99}) beyond that obtained from the manufacturer's standard FWF echoes (Section 4.2).

https://doi.org/10.5194/egusphere-2026-724
Preprint. Discussion started: 31 March 2026

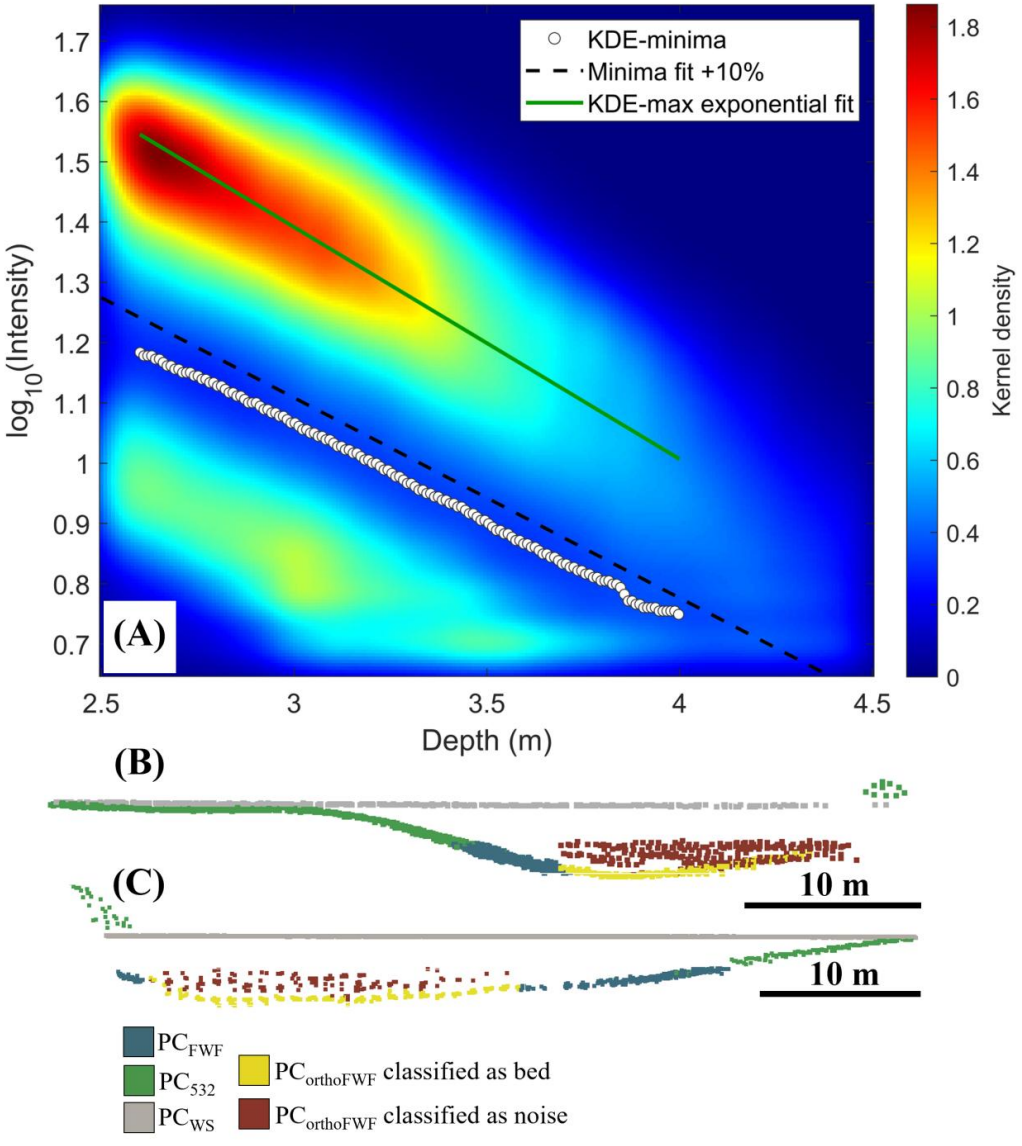

Fig. 6. Results of the filtering method used to detect the channel bed in noisy OrthoFWF echo data. (A) Semi-log plot of intensity versus depth showing a 2D kernel density estimate of all OrthoFWF echoes (N = 1,301,204) for depths > 2.5 m. Two modes are distinguished: bed echoes and noise. Local minima between the modes (white circles) were identified from 2.7 to 4.0 m and fitted with an exponential model to define the separation boundary; points above the boundary shifted upward by 10% were classified as bed, and those below as noise. The green curve shows the exponential fit of KDE maxima from 2.6 to 4.0 m (I_{ref} = 351, K_d = 0.4430 ± 0.0066 SE, R^2 = 0.971). (B–C) Representative cross-sections showing the separation of $PC_{OrthoFWF}$ into bed and noise.

https://doi.org/10.5194/egusphere-2026-724
Preprint. Discussion started: 31 March 2026

608

609 **4.2. Maximum depth achieved for the various type of LiDAR data**

610 Figure 7 provides a map view of the retrieved bathymetry along the 28 km gorge, illustrating the
611 spatial distribution of depth and the strong heterogeneity of channel geometry. Depth alternates
612 between shallow riffles, bars and deep pools over short along-stream distances, locally reaching
613 ~5–8 m (Fig. 7B-C). This spatial context motivates the coverage and depth-penetration metrics
614 reported below (Table 1) and the along-stream coverage patterns shown in Figure 8.

615 Table 1 summarizes the bathymetric coverage achieved at different levels of data leveraging.
616 Overall coverage increases from 70.1% with discrete echoes to 79.5% with the addition of FWF
617 echoes, and to 85.6% when OrthoFWF is included, although this final step entails lower spatial
618 resolution (~1 pt/m²). Length-weighted bathymetric coverage rises from 31.8% (discrete) to 54.7%
619 (+FWF) and 86.9% (+OrthoFWF), demonstrating substantial incremental gains from FWF and
620 OrthoFWF processing (Table 1). Leveraging FWF increases depth penetration from 2.9 m with
621 only the discrete PC_{532} data to ~4.5 m when adding the $PC_{OrthoFWF,}$ extending depth penetration by
622 55%.

623 Bathymetric coverage shows pronounced along-stream variability, fluctuating over ~1 km length
624 scales from <25% to >75% (Fig. 8). These variations are closely tied to river morphology, with the
625 lowest coverage typically occurring in deep, confined step-pool reaches and knickpoints, where
626 steep gradients, coarse substrates, and localized turbulence reduce water clarity and limit echo
627 penetration. In contrast, wider, low-gradient sections and meander bends generally exhibit higher
628 coverage. Incorporating $PC_{OrthoFWF}$ improves coverage across all geomorphic contexts, often
629 increasing local coverage from ~25% to >75% and reducing gaps in areas otherwise limited by
630 depth or channel complexity (Fig. 8).

631

632

633

634

635

636

https://doi.org/10.5194/egusphere-2026-724
Preprint. Discussion started: 31 March 2026

637 Table 1: Comparison of bathymetric data coverage and depth metrics

	Point density (pts/m²)	**[1]Max depth, D_{99} (99.9 %) [m]**	**[2]Total submerged bathymetry covered [%]**	**[3]Channel sections with complete cover (≥ 95%) [%]**
Onboard discrete echoes (PC_{532})	Mean of 19.4 pts/m²	2.88	70.1	31.8
Raw FWF reanalysis (PC_{FWF})	Identical	3.87	79.5	54.7
OrthoFWF processing (PC_{FWF})	1	4.46	85.6	86.9

638 [1]Maximum depth is estimated by the 99.9th percentile of depth distribution from a given data source. This is more
639 representative of the typical depth of laser extinction than the maximum depth.
640 [2]Calculated as the percentage of the submerged area where bathymetric data are available. This is an area-based metric,
641 obtained by identifying gaps in the bathymetric dataset and subtracting their fraction from the total submerged area.
642 [3]Calculated as the percentage of river length with at least 95% bathymetric coverage. This is a length-based metric,
643 where each channel section is assessed for coverage and only those meeting the ≥95% threshold are counted toward
644 the total.

https://doi.org/10.5194/egusphere-2026-724
Preprint. Discussion started: 31 March 2026

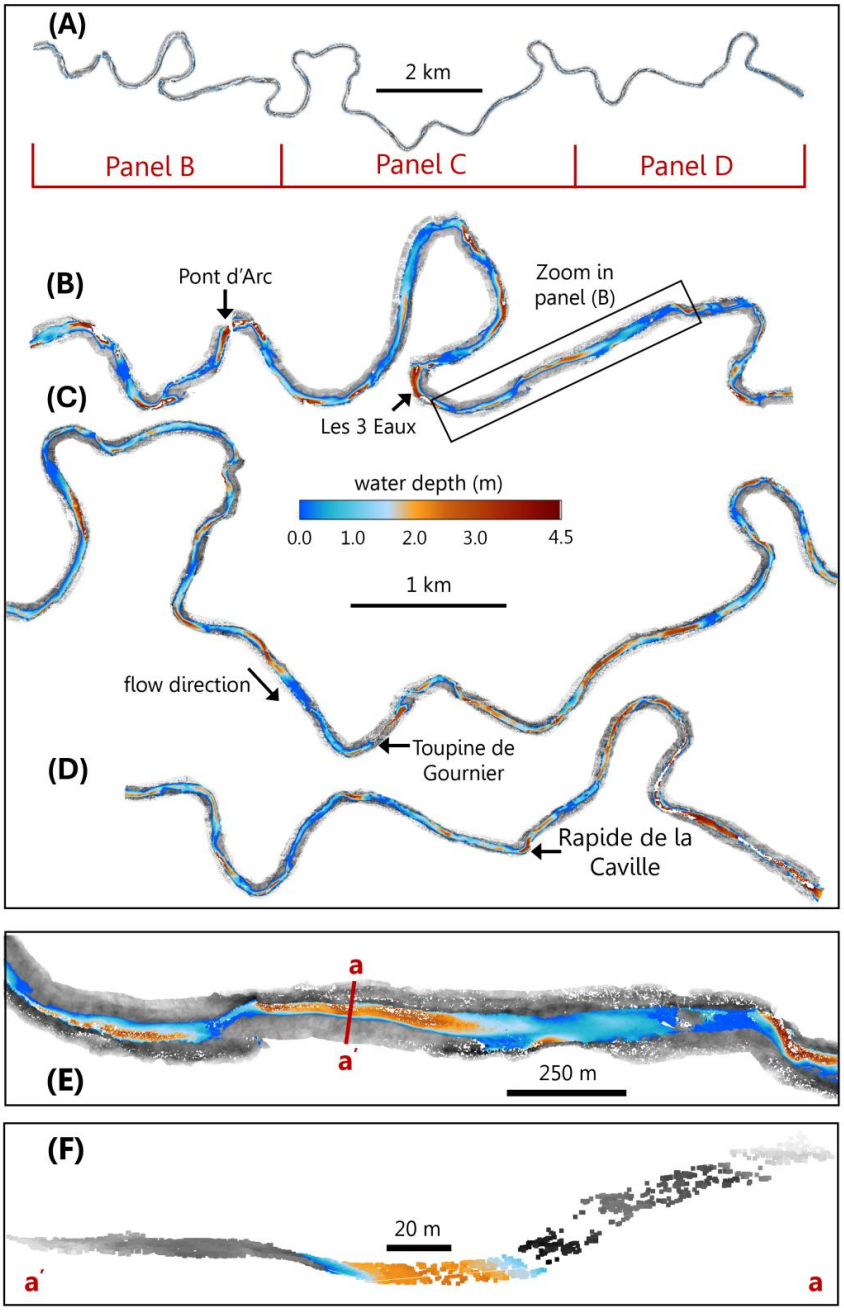

Fig. 7. Map view of the 28 km Ardèche Gorges showing LiDAR-derived bathymetry (color-coded by water depth measured on the survey day) and topography (returns above the water surface shown in grey). (A) Overview of the gorge, with three focus areas highlighted in dark red and shown in panels (B-D). Major rapids and the Pont d'Arc are indicated (see also Figs. 1 and 8). (E) Zoom-in of a straight river reach illustrating depth variability, and (F) a typical

https://doi.org/10.5194/egusphere-2026-724
Preprint. Discussion started: 31 March 2026

cross-section (location shown in E). Flow direction in panels A-E is from left to right. Surface interpolation (section 4.3) is not shown here.

645

646

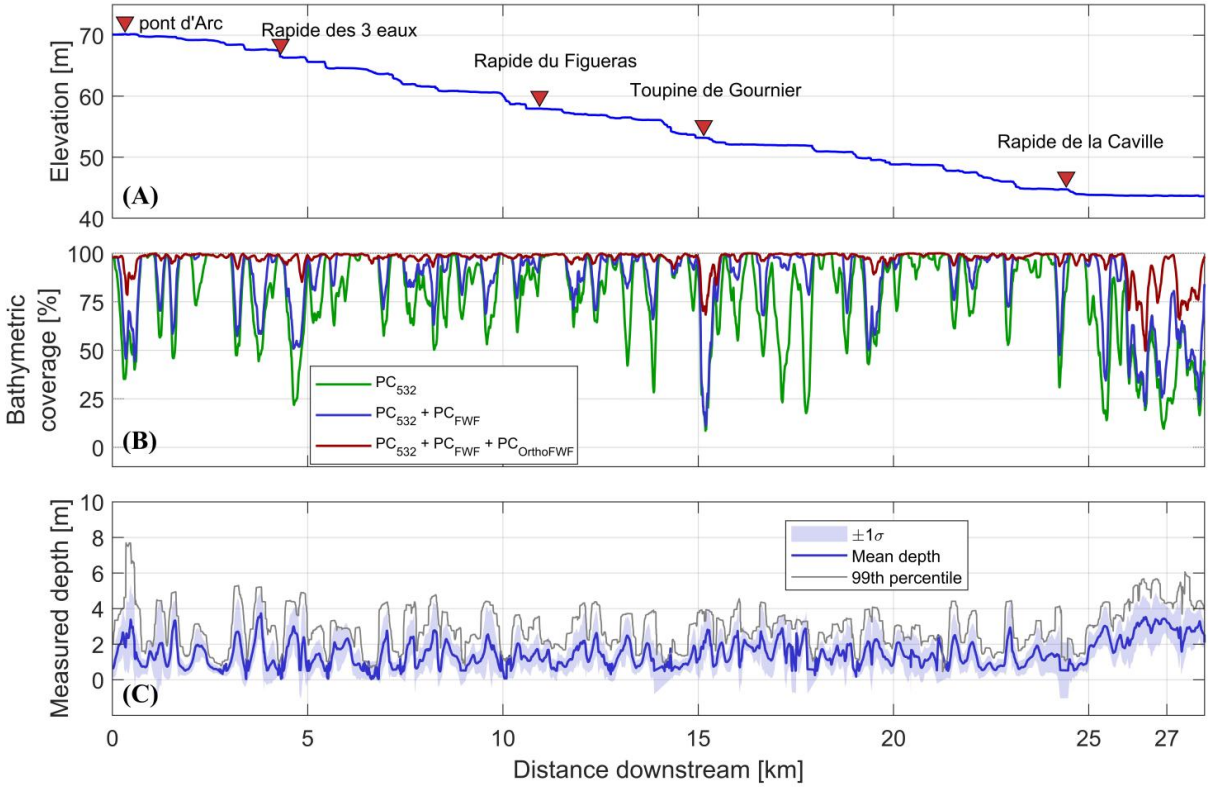

Fig. 8. Parameters derived from the topo-bathymetric dataset surveyed on 01-10-2021. (A) Water surface elevation along the Ardèche River. Red triangles mark selected rapids in the gorge. (B) Bathymetric coverage along the channel, expressed as the percentage of surrounding cells assigned to submerged-bed classes. Three processing levels are shown: PC_{532} (green), PC_{532} + PC_{FWF} (blue), and PC_{532} + PC_{FWF} + $PC_{OrthoFWF}$ (red). (C) Water-depth statistics calculated between PC_{WS} and a DEM generated by integration of the point cloud layers PC_{532}, PC_{FWF}, and $PC_{OrthoFWF}$. The solid blue line shows the mean depth, the shaded envelope represents ±1 σ, and the thin grey line shows the 99th percentile depth. The x-axis represents downstream distance from the upstream headwaters to the outlet.

647

648

https://doi.org/10.5194/egusphere-2026-724
Preprint. Discussion started: 31 March 2026

4.3. Comparison of surface generation methods for the final DEM

Figure 9 shows the statistical performance of the three surface generation methods. For PSR, the lowest mean error against $PC_{OrthoFWF}$ occurs with a Poisson resolution of 3 m and a normal scale of 10 m (Fig. 9A), although this combination yields a relatively high error standard deviation of about 1.5 m (Fig. 9B). Mean error varies non-linearly with Poisson resolution, with a minimum absolute value observed at 3m for all normal scales, which increases at higher resolutions. Larger normal scales generally produce smaller absolute mean errors. In contrast, the error standard deviation increases almost linearly with Poisson resolution. The smallest standard deviation (~1.2 m) occurs when both normal scale and Poisson resolution are set to 3 m, though this setting produces a mean error of about 0.5 m.

Compared with PSR, kriging and linear interpolation consistently produce lower error standard deviations but higher mean errors (approximately –0.75 m for kriging and –0.6 m for linear interpolation). Their error metrics remain constant because they are not influenced by normal scale or Poisson resolution. The linear and kriging methods produce inconsistent bathymetric features (Fig. 9C) which do not mimic the expected smooth transitions of individual fluvial cross-sections. On the other hand, the PSR produces smoother cross-sections with curvature magnitude and angles that are observed to be controlled by the two main parameters we explored.

https://doi.org/10.5194/egusphere-2026-724
Preprint. Discussion started: 31 March 2026

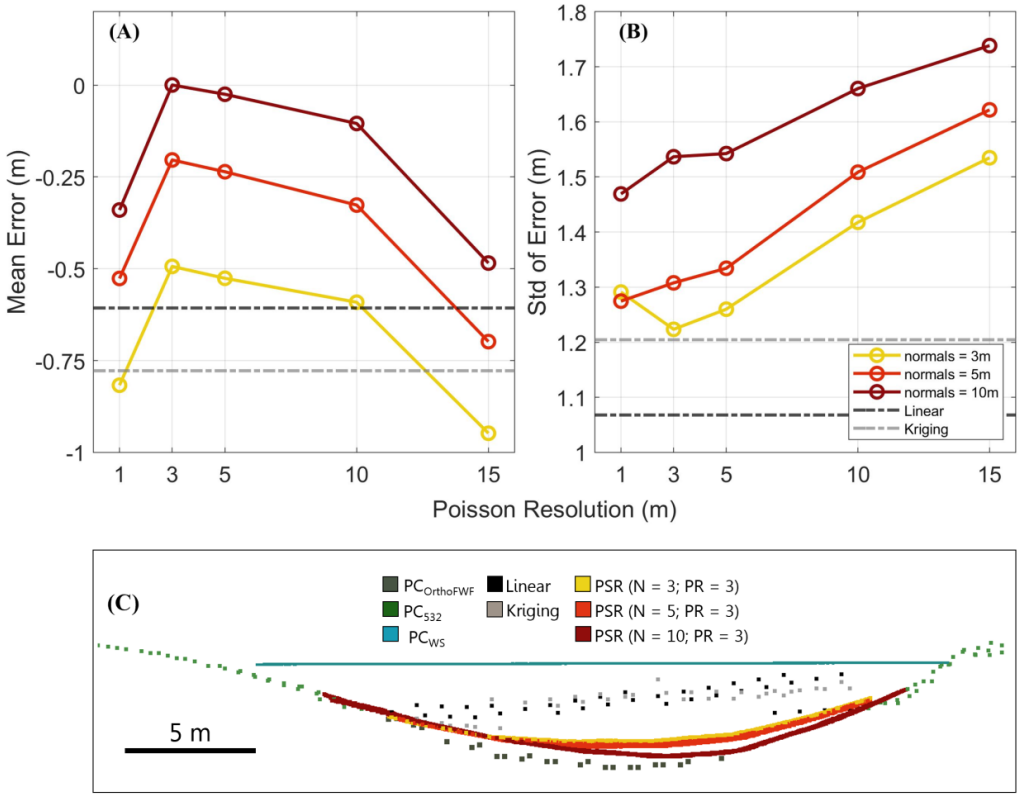

Fig. 9: Mean error (A) and error standard deviation (B) for several interpolation methods, evaluated against the $PC_{OrthoFWF}$ reference point cloud. (C) Representative cross-section of the Ardèche River comparing kriging, linear interpolation, and PSR to the $PC_{OrthoFWF}$ bathymetry; for PSR, sensitivity to the normal-estimation radius (N) and Poisson resolution (PR) is shown. These comparisons use a reduced-coverage dataset to test plausible interpolation choices, whereas the final DEM is generated from the denser full-waveform (FWF) point cloud.

667

668 **4.4 Benefits of the sonar data in gorge sections with limited TBL data**

669 We assess the impact of incorporating sonar soundings guidance into bathymetry interpolation in
670 the deepest parts of the gorge – the *Toupine de Gournier* (Fig. 10). Because bathymetric LiDAR
671 returns are largely absent in pools reaching ~8 m depth, PSR based solely on TBL data tends to
672 underestimate the actual depth (Fig. 10A), but adding the sonar point cloud significantly reduces

https://doi.org/10.5194/egusphere-2026-724
Preprint. Discussion started: 31 March 2026

these errors. In extreme cases, the vertical difference between PSR results with and without sonar reaches 5 m.

Including sonar data does not only produce more realistic depth estimates but also constrains the underwater cross-section to a more sensible geometry with regard to the river's water surface (Fig. 10A). A map-view comparison in the *Toupine de Gournier* further shows that, whereas PSR generates a smooth and continuous depth pattern, linear interpolation yields spatially inconsistent and discontinuous bathymetry in these data-sparse areas (Fig. 10B, C). These results highlight that even low spatial resolution sonar measurements provide essential anchoring constraints to guide bathymetric interpolation magnitude and shape in the deepest sections of the gorge, where LiDAR alone proves insufficient.

https://doi.org/10.5194/egusphere-2026-724
Preprint. Discussion started: 31 March 2026

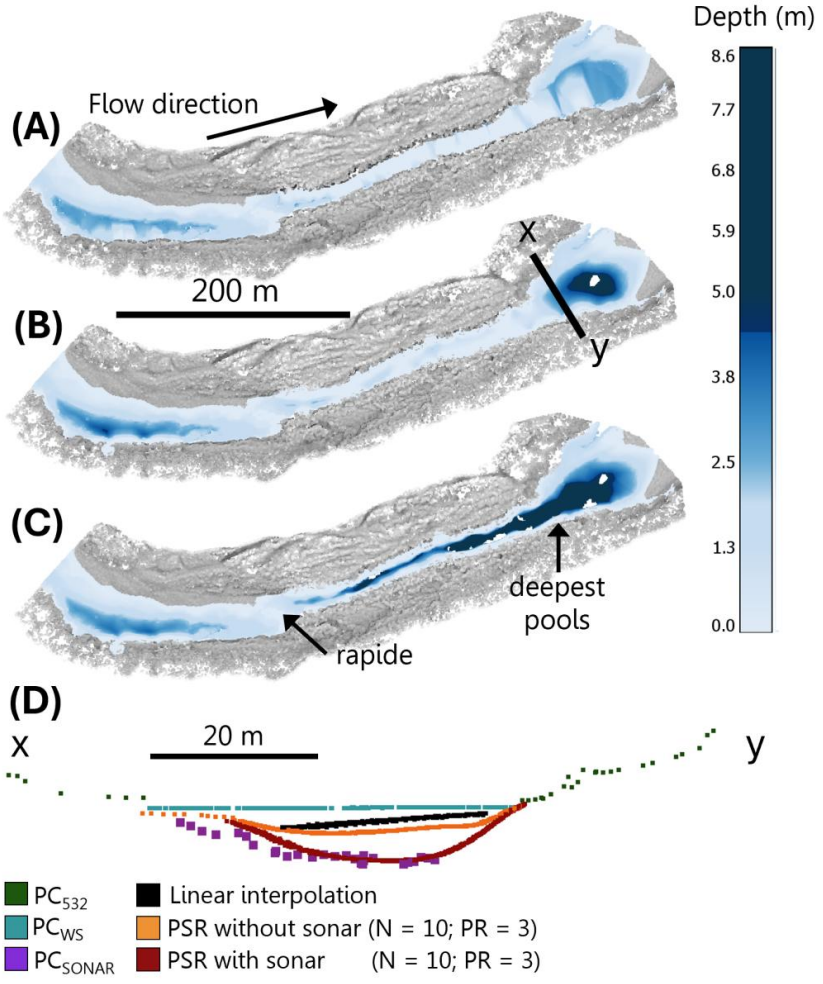

Fig. 10. Effect of incorporating sonar data into Poisson-reconstructed (PSR) bathymetry at the Toupine de Gournier rapid in the Ardèche Gorges, where pools reach about 8 m depth. In this deep reach, LiDAR bathymetry is largely missing, and sonar helps constrain reconstruction. (A) Linear interpolation. (B) PSR without sonar (C) PSR with sonar. The shared depth legend shows maximum depths increasing from about 3 m in A to 5.3 m in B and 8.6 m in C. (D) Cross-section through a deep pool (location in B), showing that PSR with sonar better captures pool geometry than PSR without sonar or linear interpolation.

695

https://doi.org/10.5194/egusphere-2026-724
Preprint. Discussion started: 31 March 2026

5. Discussion

5.1 Quality, completeness, and limitations of the final DEM

Topo-bathymetric LiDAR proved capable of producing a near-continuous DEM over the 28-km Ardèche River Gorges, despite its variable depth and hydraulic conditions. Thanks to clear water at the time of acquisition, with the attenuation coefficient for the 532 nm channel estimated at $K_{d,532} = 0.39\ m^{-1}$, both discrete and FWF returns of the 532 nm channel captured most of the bed morphology in shallow to moderate depths. This value lies at the lower end of the range observed in French rivers surveyed by our team ($K_{d,532} = 0.25–1.2\ m^{-1}$), which helps explain the favorable depth penetration achieved here (Lague and Feldman, 2020). Because attenuation coefficients are rarely reported in airborne river-bathymetry studies, direct cross-study comparisons remain difficult.

Integrating discrete returns, reprocessed FWF, and OrthoFWF data allowed us to reach 85-87% bathymetric areal coverage, with complete or near-complete coverage (>95%) over 86.9% of the river length. In narrower and/or more turbid rivers, prior studies commonly highlight more spatially patchy bed detection and stronger depth- and turbidity-related limitations on optical retrieval (e.g., Mandlburger et al., 2015; Tonina et al., 2019; Pan et al., 2016).

Data quality is not spatially uniform, however. Coverage decreases progressively with depth, reflecting the expected attenuation of the green laser. Depth penetration increases from 2.9 m with discrete returns to 4.5 m with OrthoFWF (Table 1), which explains the improved completeness in deeper sections (Fig. 8B). This progressive depth-dependent decline is consistent with trends reported in previous airborne bathymetry studies (e.g., Hilldale & Raff, 2008; Lague & Feldman, 2020) and underpins the effectiveness of the unsupervised intensity-based classification used here (Fig. 6).

Although the complementary sonar survey improved representation of the deepest sections, its influence on the final DEM remains modest because LiDAR coverage was already high over most of the gorge (Table 1). The sonar mainly affects a small number of deep pools where LiDAR sampling is sparse. Overall, the dataset can be considered of high quality, and the sonar should be viewed as a targeted supplement rather than a primary data contributor.

https://doi.org/10.5194/egusphere-2026-724
Preprint. Discussion started: 31 March 2026

5.2 Methodological developments

5.2.1 Full-waveform extraction and OrthoFWF generation

A central contribution of this study is demonstrating how combining FWF reprocessing with orthorectified waveform synthesis (OrthoFWF) substantially increases depth penetration and spatial continuity (Table 1; Figs. 5, 6, 8). Earlier work highlighted the value of FWF for recovering missed bed echoes (e.g., Zhao et al., 2022; Mallet & Bretar, 2009; Höfle et al., 2012; Kogut and Bakuła2019), but applications in fluvial systems remain limited (Pan et al., 2015; Mandlburger et al., 2015; Lague & Feldman, 2020; Mader et al., 2023b). Our results confirm and extend these findings: reprocessed FWF may recover bathymetric returns, which the onboard discrete acquisition process missed, thereby adding a substantial increment in both depth and spatial coverage. Indeed, thanks to OrthoFWF processing we increase the maximum depth measured from 2.88 m to 4.46 m, a significant leap also observed by Mader et al. (2023b) in turbid water (+ 0.55 m). In riverine environments where high measurement density and high spatial resolution are needed for accurate modelling, this ability to obtain enhanced coverage without employing larger footprint systems is essential (Godet et al., 2025).

A second new development is the unsupervised, intensity-based separation of green bottom echoes from misclassified returns in the OrthoFWF domain (Fig. 6). After generating the OrthoFWF raster through stacking numerous waveform samples (Fig. 5) - a process that enhances the signal-to-noise ratio and clarifies extinction patterns - we derive a deterministic intensity threshold using a two-dimensional kernel density representation of the relationship between intensity and water depth. The large dataset (~1.3 million points), when evaluated through this kernel density framework, reveals locally concentrated regions of high point density that correspond to coherent physical signals and thereby provide a robust basis for threshold selection. Applying the resulting threshold to the OrthoFWF raster produces a clean and stable separation of bed signals from noise (Fig. 6B, C), even prior to any manual refinement. The removal of low-intensity noise further strengthens the effective signal-to-noise ratio and supports more reliable depth extraction in deeper or optically complex environments.

5.2.2 Interpolation of bathymetric gaps

Interpolating bathymetric LiDAR data in rivers is challenging because river corridors are highly anisotropic and follow curvilinear paths, making conventional methods such as linear interpolation

https://doi.org/10.5194/egusphere-2026-724
Preprint. Discussion started: 31 March 2026

or isotropic kriging poorly suited (e.g., Bailly et al., 2010). Nonetheless, for bathymetric surveys involving very large datasets, linear interpolation (Mandlburger et al., 2015) and kriging (e.g., Hilldale and Raff, 2008; Legleiter and Kyriakidis, 2008; McKean et al., 2009) are still among the most widely used approaches. River-adapted methods (e.g., Legleiter & Kyriakidis, 2008) generally outperform standard interpolation in shallow or geomorphologically complex environments and are essential for producing reliable error estimates.

The use of Poisson Surface Reconstruction (PSR) in riverine bathymetry is novel. Since its introduction (Kazhdan et al., 2006), PSR has mainly been applied to terrestrial applications such as landslide mapping (Gupka and Shukla, 2018), but its ability to generate continuous surfaces that preserve realistic local curvature and slope transitions across data gaps makes it promising for river environments. However, PSR is a geometric reconstruction method and may oversmooth where observations are sparse; therefore, it may be coupled with numerical shallow-water simulations to further constrain hydraulically plausible bathymetric geometry (e.g., Gessese et al., 2011).

Within this context, our interpolation analysis reveals clear trade-offs between methods. The goal of a morphologically coherent reconstruction is to produce a continuous bed with realistic curvature and slope transitions, thereby minimizing hydraulic pathologies in subsequent modeling (e.g., spurious jumps, discontinuities, over-smoothing, or truncated depth extremes). PSR best meets this objective, producing the most morphologically realistic surfaces and the lowest systematic bias, although it is sensitive to parameterization and exhibits somewhat higher variance. In contrast, kriging and linear interpolation yield more stable predictions but tend to over-smooth the bed, introduce artifacts, and generate hydraulically unrealistic bathymetry, limitations also noted in fluvial and hydraulic modeling studies (e.g., Legleiter & Kyriakidis, 2008; Brasington et al., 2012).

Incorporating sonar points in deep pools reduces major biases; in extreme cases, PSR differs by up to 5 m with and without sonar (Fig. 10). These corrections, however, remain spatially limited and only matter where LiDAR data are absent, consistent with findings that even sparse sonar soundings can strongly constrain interpolation in optically challenging reaches (Hilldale & Raff, 2008).

Overall, our results indicate that PSR is best suited when morphological realism is required (e.g., for hydraulic modeling), whereas kriging and linear interpolation offer stability at the cost of

https://doi.org/10.5194/egusphere-2026-724
Preprint. Discussion started: 31 March 2026

oversimplified or unrealistic channel forms. Sonar data is most valuable in the deepest sections, where even OrthoFWF provides insufficient coverage, primarily helping maintain plausible depth structure.

5.3 Practical considerations and workflow implementation

The workflow (Fig. 3) is modular rather than fully automated. Pre-processing in Python minimizes memory load and enables efficient filtering, while CloudCompare provides essential visual-inspection tools for validating classification, depth extraction, and waveform behavior. The newly introduced qFWF plugin constitutes a major step toward accessible FWF processing, supporting both exploration and large-scale batch processing. As it is open-source, future improvements, such as more advanced echo-detection algorithms can be integrated.

We also highlight the utility of 3DMASC (Letard et al., 2024), a powerful machine-learning classification tool tailored for topo-bathymetric LiDAR, available both through CloudCompare's graphical interface and as a Python implementation. In combination, CloudCompare's ability to load FWF data, inspect echo structure, manipulate files in 3D, and extract waveform components makes it one of the most capable platforms currently available for FWF-based bathymetric processing.

Although demonstrated in a narrow gorge, the workflow is applicable to a wide range of fluvial systems. Wider or more turbid rivers may require additional vegetation filtering, integration with multispectral UAV imagery, or tighter survey-timing constraints to maximize water clarity. As emphasized in previous work, survey timing remains one of the most critical factors governing the success of green-LiDAR bathymetry (Lague & Feldman, 2020).

Beyond the methodological gains in coverage, the key scientific value of topo-bathymetric LiDAR is that it provides a continuous description of the river corridor bed**,** whether as point clouds or gridded products**,** linking floodplain, banks, and the submerged channel rather than truncating information at the waterline. In confined systems such as the Ardèche gorges, deep pools, scour zones, and the thalweg strongly control conveyance, flow structure, and habitat, yet these geometries are largely absent from topo-only products (e.g., LiDAR HD). Our topo-bathymetric bed description therefore reveals coherent submerged morphology and bedforms that would otherwise remain invisible, including organized bed undulations and pool–riffle transitions in

https://doi.org/10.5194/egusphere-2026-724
Preprint. Discussion started: 31 March 2026

deeper sections (Fig. 11), providing direct constraints for geomorphic interpretation and more realistic inputs for hydraulic modelling.

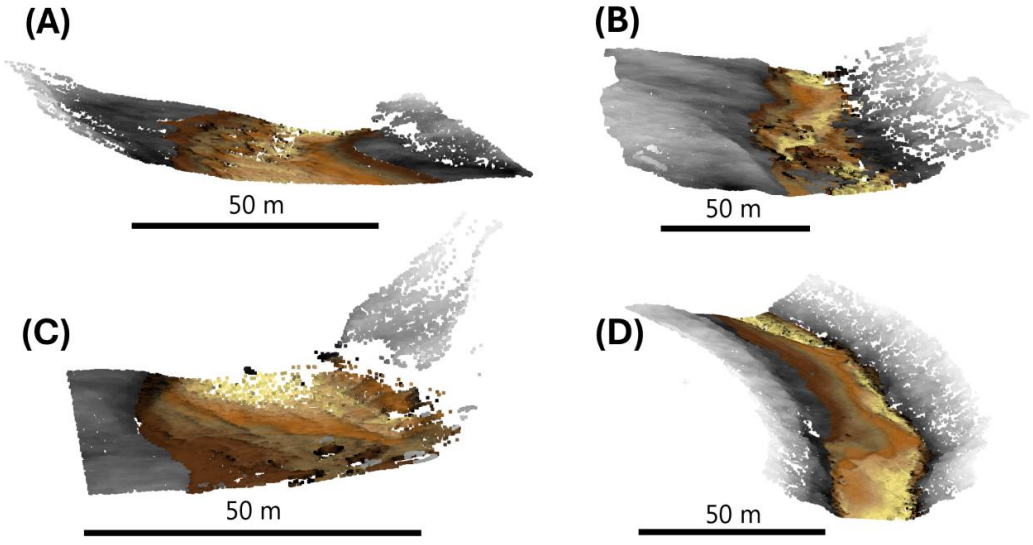

Fig. 11. Representative bed morphologies from the topo-bathymetric LiDAR survey of the Ardèche River gorges. (A–D) Four reaches where bathymetric elevation reveals organized bedforms and bed morphology. Grey shows ground points in emerged areas from the combined PC_{1064} and PC_{532} point clouds; white indicates missing returns.

https://doi.org/10.5194/egusphere-2026-724
Preprint. Discussion started: 31 March 2026

6. Conclusion

This study demonstrates that large-scale airborne Topo-Bathymetric LiDAR, when coupled with targeted methodological advances, can deliver river bathymetry of sufficient completeness and morphological fidelity to support demanding hydraulic and geomorphological applications in high-energy, confined settings. Working in the Ardèche River Gorges, we show that many of the long-standing limitations of green LiDAR in deep, complex channels can be substantially reduced. This is achieved not only by adapting acquisition conditions, but, critically, by redesigning the processing chain from waveform to DEM.

By integrating discrete and full-waveform LiDAR with an OrthoFWF synthesis, we extend effective depth penetration and increase both areal and longitudinal coverage of submerged topography to levels that would be difficult to achieve with discrete data alone. The unsupervised, intensity-based classification and the 3DMASC random-forest bathymetric classifier together illustrate that physically informed, data-driven methods can robustly distinguish actual bed returns from noise, reducing the need for subjective, site-specific tuning. In parallel, the comparison of interpolation strategies highlights that Poisson surface reconstruction, when carefully parameterized and constrained by sparse but strategic sonar soundings, best preserves small-scale morphological structures while maintaining hydraulic continuity at the reach scale.

Beyond the technical gains, the workflow provides a transferable template for practitioners facing similar constraints: clear-water windows of opportunity, complex topography, and the requirement for near-continuous bathymetric surfaces for modeling floods, sediment transport, or habitat mapping. The approach emphasizes that achieving high-quality river DEMs is not the result of a single algorithmic choice, but of coordinated decisions on acquisition, waveform handling, classification, data fusion, and surface reconstruction that collectively determine the reliability of the final product.

Remaining limitations point to fertile directions for future work. Refinement of waveform decomposition and intensity calibration could further enhance depth retrieval in turbid or deeper waters, while closer temporal coordination with complementary sonar or UAV-based surveys would reduce uncertainties in deep pools and rapidly evolving reaches. Extending and validating the workflow across rivers with varying optical, hydraulic, and geomorphic conditions will be essential to test its generality and develop guidelines for its broader adoption.

https://doi.org/10.5194/egusphere-2026-724
Preprint. Discussion started: 31 March 2026

Overall, this study underscores the maturing role of Topo-Bathymetric LiDAR as a core technology for fluvial science and river management. When paired with advanced processing and targeted ground truth, TBL can now deliver basin-scale, hydraulically consistent representations of river corridors that were previously impractical to obtain, thereby opening new possibilities for monitoring geomorphic change, improving hazard assessments, and supporting evidence-based river restoration and conservation.

Acknowledgments

We thank Shlomy Vainer, Sophie Rothman, and Stephane Bonnet for their valuable assistance during field mission, and the GEOFIT team for airborne LiDAR data acquisition (Cyril Michon, William Gentile and Emmanuel Gouraud). This research has been supported by the H2020 European Research Council (grant no. 803721; project FEASIBLe) and the Agence Nationale de la Recherche (grant ANR-18-CE01-00; project TopoExtreme; grant ANR-17-CE03-0011; project PICS). RN was supported by the Brittany Regional *Bienvenüe* 2024 CHANGING fellowship. The Titan DW sensor, operated by the Nantes-Rennes Lidar Platform has been funded by the Region Pays de la Loire with funding of the RS2E-OSUNA programs and the Region Bretagne with support from the European Regional Development Fund. We gratefully acknowledge the authorities of the Réserve Naturelle Nationale des Gorges de l'Ardèche (France) for logistical support and authorization to conduct airborne acquisition. AI-based language tools were used to help refine the writing.

Data Availability

The classified point clouds and final DEM will be made available for download upon publication. The qFWF plugin (Lague et al., 2025) will be made available in CloudCompare upon publication. Daily mean discharge data are publicly available from the French national hydrological database (Hydro Portail, station V5064010 – Ardèche at Saint-Martin-d'Ardèche): https://www.hydro.eaufrance.fr/station/V5064010.

Contribution Statement

DL and PS conceptualized the LiDAR survey. TB, PL, and DL processed the raw data using StripAlign for georeferencing. PL and DL applied refraction corrections and conducted the initial

https://doi.org/10.5194/egusphere-2026-724
Preprint. Discussion started: 31 March 2026

orthoFWF processing. DGM, DL and PL developed the qFWF plugin. RN, in collaboration with DL, designed the overall data processing strategy. RN then carried out the full data processing and analysis, prepared all figures, and led the writing of the manuscript. PS, DL, VG, RC and OP contributed to the acquisition of the financial support for the projects leading to this publication. All authors reviewed and provided feedback on the manuscript drafts.

Competing interests

The authors declare that they have no conflict of interest.

https://doi.org/10.5194/egusphere-2026-724
Preprint. Discussion started: 31 March 2026

References

Abady, L., Bailly, J. S., Baghdadi, N., Pastol, Y., and Abdallah, H.: Assessment of quadrilateral fitting of the water column contribution in lidar waveforms on bathymetry estimates, IEEE Geosci. Remote Sens. Lett., 11, 813–817, https://doi.org/10.1109/LGRS.2013.2279271, 2014.

Abdallah, H., Baghdadi, N., Bailly, J. S., Pastol, Y., and Fabre, F.: Wa-LiD: A new LiDAR simulator for waters, IEEE Geosci. Remote Sens. Lett., 9, 744–748, https://doi.org/10.1109/LGRS.2011.2180506, 2012.

Andersen, M. S., Gergely, Á., Al-Hamdani, Z., Steinbacher, F., Larsen, L. R., and Ernstsen, V. B.: Processing and performance of topobathymetric lidar data for geomorphometric and morphological classification in a high-energy tidal environment, Hydrol. Earth Syst. Sci., 21, 43–63, https://doi.org/10.5194/hess-21-43-2017, 2017.

Anees, M. T., Abdullah, K., Nawawi, M. N. M., Ab Rahman, N. N. N., Piah, A. R. M., Zakaria, N. A., and Omar, A. M.: Numerical modeling techniques for flood analysis, J. Afr. Earth Sci., 124, 478–486, https://doi.org/10.1016/j.jafrearsci.2016.10.001, 2016.

Bailly, J. S., Le Coarer, Y., Languille, P., Stigermark, C. J., and Allouis, T.: Geostatistical estimations of bathymetric LiDAR errors on rivers, Earth Surf. Proc. Land., 35, 1199–1210, https://doi.org/10.1002/esp.1991, 2010.

Baker, V. R.: Stream-channel response to floods, with examples from central Texas, Geol. Soc. Am. Bull., 88, 1057–1071, https://doi.org/10.1130/0016-7606(1977)88<1057:SRTFWE>2.0.CO;2, 1977.

Bernard, T. G., Lague, D., and Steer, P.: Beyond 2D landslide inventories and their rollover: synoptic 3D inventories and volume from repeat lidar data, Earth Surf. Dynam., 9, 1013–1044, https://doi.org/10.5194/esurf-9-1013-2021, 2021.

Blais, J. A. R., He, K., and Larouche, C.: Evolutionary spatial modeling of creosote sites on the Bow River, Calgary, Alberta, in: Digital Image Processing and Visual Communications Technologies in the Earth and Atmospheric Sciences II, Vol. 1819, SPIE, 103–112, https://doi.org/10.1117/12.142191, 1993.

Brasington, J., Rumsby, B. T., and McVey, R. A.: Monitoring and modelling morphological change in a braided gravel-bed river using high resolution GPS-based survey, Earth Surf. Proc. Land., 25, 973–990, https://doi.org/10.1002/1096-9837(200008)25:9<973::AID-ESP111>3.0.CO;2-Y, 2000.

Coppo Frias, M., Vesterhauge, A. R., Olesen, D. H., Bandini, F., Grosen, H., Nielsen, S. Y., and Bauer-Gottwein, P.: Combining UAS LiDAR, sonar, and radar altimetry for river hydraulic characterization, Drones, 9, 31, https://doi.org/10.3390/drones9010031, 2025.

Fernandez-Diaz, J. C., Glennie, C. L., Carter, W. E., Shrestha, R. L., Sartori, M. P., Singhania, A., Legleiter, C. J., and Overstreet, B. T.: Early results of simultaneous terrain and shallow water bathymetry mapping using a single-wavelength airborne LiDAR sensor, IEEE J. Sel. Top. Appl. Earth Obs. Remote Sens., 7, 623–635, https://doi.org/10.1109/JSTARS.2013.2265255, 2014.

Frizzle, C., Trudel, M., Daniel, S., Pruneau, A., and Noman, J.: LiDAR topo-bathymetry for riverbed elevation assessment: A review of approaches and performance for hydrodynamic modelling of flood plains, Earth Surf. Proc. Land., 49, 2585–2600, https://doi.org/10.1002/esp.5808, 2024.

Genuite, K., Delannoy, J. J., Bahain, J. J., Gresse, M., Jaillet, S., Philippe, A., Pons-Branchu, E., Revil, A., and Voinchet, P.: Dating the landscape evolution around the Chauvet-Pont d'Arc cave, Sci. Rep., 11, 8944, https://doi.org/10.1038/s41598-021-88240-5, 2021.

Gessese, A. F., Sellier, M., Van Houten, E., and Smart, G.: Reconstruction of river bed topography from free surface data using a direct numerical approach in one-dimensional shallow water flow, Inverse Probl., 27, 025001, https://doi.org/10.1088/0266-5611/27/2/025001, 2011.

Girardeau-Montaut, D.: CloudCompare [code], EDF R&D Telecom ParisTech, France, available at: http://www.cloudcompare.org (last access: 11 March 2026), 2016.

https://doi.org/10.5194/egusphere-2026-724
Preprint. Discussion started: 31 March 2026

Girardeau-Montaut, D.: CloudCompare (Version 2.14.alpha) [code], available at: http://www.cloudcompare.org (last access: 11 March 2026), 2025.

Godet, J., Nicolle, P., Hocini, N., Gaume, E., Davy, P., Pons, F., Javelle, P., Garambois, P.-A., Lague, D., and Payrastre, O.: Benchmark dataset for hydraulic simulations of flash floods in the French Mediterranean region, Earth Syst. Sci. Data, 17, 2963–2983, https://doi.org/10.5194/essd-17-2963-2025, 2025.

Gordon, N. D., McMahon, T. A., Finlayson, B. L., Gippel, C. J., and Nathan, R. J.: Stream Hydrology: An Introduction for Ecologists, 2nd edn., Wiley, Chichester, UK, https://doi.org/10.1604/9780470843581, 2004.

Grant, G. E., Swanson, F. J., and Wolman, M. G.: Pattern and origin of stepped-bed morphology in high-gradient streams, Western Cascades, Oregon, Geol. Soc. Am. Bull., 102, 340–352, https://doi.org/10.1130/0016-7606(1990)102<0340:PAOOSB>2.3.CO;2, 1990.

Guenther, G. C.: Airborne laser hydrography: System design and performance factors, NOAA Professional Paper Series, 1, National Ocean Service, 1985.

Guenther, G. C. and Mesick, H. C.: Analysis of airborne laser hydrography waveforms, in: Ocean Optics IX, edited by: Blizard, M. A., Vol. 0925, SPIE, 232–241, https://doi.org/10.1117/12.945729, 1988.

Guenther, G. C., Cunningham, A. G., Larocque, P. E., Reid, D. J., Service, N. O., Highway, E., and Spring, S.: Meeting the accuracy challenge in airborne lidar bathymetry, EARSeL eProceedings, 1, 1–27, 2000.

Guenther, G. C., Brooks, M. W., and LaRocque, P. E.: New capabilities of the "SHOALS" airborne lidar bathymeter, Remote Sens. Environ., 73, 247–255, https://doi.org/10.1016/S0034-4257(00)00099-7, 2000.

Gupta, S. K. and Shukla, D. P.: Application of drone for landslide mapping, dimension estimation and its 3D reconstruction, J. Indian Soc. Remote Sens., 46, 903–914, https://doi.org/10.1007/s12524-017-0727-1, 2018.

Guo, Q., Li, W., Yu, H., and Alvarez, O.: Effects of topographic variability and lidar sampling density on several DEM interpolation methods, Photogramm. Eng. Remote Sens., 76, 701–712, https://doi.org/10.14358/PERS.76.6.701, 2010.

Heritage, G. L., Milan, D. J., Large, A. R. G., and Fuller, I. C.: Influence of survey strategy and interpolation model on DEM quality, Geomorphology, 112, 334–344, https://doi.org/10.1016/j.geomorph.2009.06.024, 2009.

Hickman, G. D. and Hogg, J. E.: Application of an airborne pulsed laser for near shore bathymetric measurements, Remote Sens. Environ., 1, 47–58, https://doi.org/10.1016/S0034-4257(69)90088-1, 1969.

Hilldale, R. C. and Raff, D.: Assessing the ability of airborne LiDAR to map river bathymetry, Earth Surf. Proc. Land., 33, 773–783, https://doi.org/10.1002/esp.1575, 2008.

Höfle, B., Vetter, M., Pfeifer, N., Mandlburger, G., and Stötter, J.: Water surface mapping from airborne laser scanning using signal intensity and elevation data, Earth Surf. Proc. Land., 34, 1635–1649, https://doi.org/10.1002/esp.1853, 2009.

Hug, C., Krzystek, P., and Fuchs, W.: Advanced lidar data processing with LasTools, in: XXth ISPRS Congress, 12–23, 2004.

Hydro Portail: Station V5064010 – Ardèche at Saint-Martin-d'Ardèche, French national portal for hydrological data, available at: https://www.hydro.eaufrance.fr/station/V5064010 (last access: 11 March 2026), 2025.

Islam, M. T., Yoshida, K., Nishiyama, S., Sakai, K., and Tsuda, T.: Characterizing vegetated rivers using novel unmanned aerial vehicle-borne topo-bathymetric green lidar: Seasonal applications and challenges, River Res. Appl., 38, 44–58, https://doi.org/10.1002/rra.3875, 2022.

Kazhdan, M., Bolitho, M., and Hoppe, H.: Poisson surface reconstruction, in: Proceedings of the Fourth Eurographics Symposium on Geometry Processing, 61–70, https://doi.org/10.2312/SGP/SGP06/061-070, 2006.

Kogut, T. and Bakuła, K.: Improvement of full waveform airborne laser bathymetry data processing based on waves of neighborhood points, Remote Sens., 11, 1255, https://doi.org/10.3390/RS11101255, 2019.

https://doi.org/10.5194/egusphere-2026-724
Preprint. Discussion started: 31 March 2026

992 Krabill, W. B., Collins, J. G., Link, L. E., Swift, R. N., and Butler, M. L.: Airborne laser topographic mapping results,
993 Photogramm. Eng. Remote Sens., 50, 685–694, 1984.

994 Lague, D. and Feldmann, B.: Topo-bathymetric airborne LiDAR for fluvial-geomorphology analysis, in:
995 Developments in Earth Surface Processes, Vol. 23, Elsevier, 25–54, https://doi.org/10.1016/B978-0-444-64177-
996 9.00002-3, 2020.

997 Lague, D., Brodu, N., and Leroux, J.: Accurate 3D comparison of complex topography with terrestrial laser scanner:
998 Application to the Rangitikei canyon (NZ), ISPRS J. Photogramm. Remote Sens., 82, 10–26,
999 https://doi.org/10.1016/j.isprsjprs.2013.04.009, 2013.

1000 Lague, D., Girardeau-Montaut, D., and Leroy, P.: Full waveform plugin for CloudCompare [code], Univ Rennes,
1001 CNRS, LiDAR Platform, OSERen, UAR 3343, Rennes, France, https://doi.org/10.26169/fwf, 2025.

1002 Lang, M., Naulet, R., Recking, A., Cœur, D., and Gigon, C.: Etude de cas: l'analyse des pluies et crues extrêmes
1003 observées depuis 200 ans dans un bassin cévenol, l'Ardèche, La Houille Blanche, 88, 131–138,
1004 https://doi.org/10.1051/lhb/2002097, 2002.

1005 Le Lay, M. and Saulnier, G. M.: Exploring the signature of climate and landscape spatial variabilities in flash flood
1006 events: Case of the 8–9 September 2002 Cévennes-Vivarais catastrophic event, Geophys. Res. Lett., 34,
1007 https://doi.org/10.1029/2007GL029746, 2007.

1008 Leopold, L. B. and Wolman, M. G.: River channel patterns: Braided, meandering, and straight, U.S. Geological Survey
1009 Professional Paper 282-B, U.S. Government Printing Office, Washington, D.C., 1957.

1010 Letard, M., Collin, A., Corpetti, T., Lague, D., Pastol, Y., Gloria, H., and Mury, A.: Classification of coastal and
1011 estuarine ecosystems using full-waveform topo-bathymetric lidar data and artificial intelligence, in: OCEANS 2021:
1012 San Diego–Porto, IEEE, 1–10, https://doi.org/10.23919/OCEANS44145.2021.9705797, 2021.

1013 Letard, M., Collin, A., Corpetti, T., Lague, D., Pastol, Y., and Ekelund, A.: Classification of land-water continuum
1014 habitats using exclusively airborne topobathymetric LiDAR green waveforms and infrared intensity point clouds,
1015 Remote Sens., 14, 341, https://doi.org/10.3390/rs14020341, 2022.

1016 Letard, M., Lague, D., Le Guennec, A., Lefèvre, S., Feldmann, B., Leroy, P., and Corpetti, T.: 3DMASC: Accessible,
1017 explainable 3D point clouds classification. Application to bi-spectral topo-bathymetric lidar data, ISPRS J.
1018 Photogramm. Remote Sens., 207, 175–197, https://doi.org/10.1016/j.isprsjprs.2023.11.022, 2024.

1019 Liu, X.: Airborne LiDAR for DEM generation: some critical issues, Prog. Phys. Geogr., 32, 31–49,
1020 https://doi.org/10.1177/0309133308089496, 2008.

1021 Mader, D., Richter, K., Westfeld, P., Weiß, R., and Maas, H. G.: Detection and extraction of water bottom topography
1022 from laser bathymetry data by using full-waveform-stacking techniques, Int. Arch. Photogramm. Remote Sens. Spatial
1023 Inf. Sci., XLII-2/W13, 1053–1059, https://doi.org/10.5194/isprs-archives-XLII-2-W13-1053-2019, 2019.

1024 Mader, D., Richter, K., Westfeld, P., and Maas, H. G.: Potential of a non-linear full-waveform stacking technique in
1025 airborne LiDAR bathymetry: Demonstration of full-waveform stacking techniques on data from the Elbe River, PFG
1026 J. Photogramm. Remote Sens. Geoinf. Sci., 89, 139–158, https://doi.org/10.1007/s41064-021-00147-y, 2021.

1027 Mader, D., Richter, K., Westfeld, P., Nistad, J.-G., and Maas, H.-G.: Analysis of the potential of full-waveform stacking
1028 techniques applied to coastal airborne LiDAR bathymetry data of the German Wadden Sea National Park, Int. Hydrogr.
1029 Rev., 29, https://doi.org/10.58440/ihr-29-2-a31, 2023a.

1030 Mader, D., Richter, K., Westfeld, P., and Maas, H.-G.: Volumetric nonlinear ortho full-waveform stacking in airborne
1031 LiDAR bathymetry for reliable water bottom point detection in shallow waters, ISPRS J. Photogramm. Remote Sens.,
1032 204, 145–162, https://doi.org/10.1016/j.isprsjprs.2023.08.014, 2023b.

1033 Magruder, L. A., Neuenschwander, A. L., and Marmillion, S. P.: Lidar waveform stacking techniques for faint ground
1034 return extraction, J. Appl. Remote Sens., 4, 043501, https://doi.org/10.1117/1.3299657, 2010.

1035 Mallet, C. and Bretar, F.: Full-waveform topographic lidar: State-of-the-art, ISPRS J. Photogramm. Remote Sens., 64,
1036 1–16, https://doi.org/10.1016/j.isprsjprs.2008.09.007, 2009.

https://doi.org/10.5194/egusphere-2026-724
Preprint. Discussion started: 31 March 2026

Mandlburger, G., Pfennigbauer, M., and Pfeifer, N.: Analyzing near water surface penetration in laser bathymetry – A case study at the River Pielach, ISPRS Ann. Photogramm. Remote Sens. Spatial Inf. Sci., II-5/W2, 175–180, https://doi.org/10.5194/isprsannals-II-5-W2-175-2013, 2013.

Mandlburger, G., Hauer, C., Wieser, M., and Pfeifer, N.: Topo-bathymetric LiDAR for monitoring river morphodynamics and instream habitats—A case study at the Pielach River, Remote Sens., 7, 6160–6195, https://doi.org/10.3390/rs70506160, 2015.

McKean, J., Nagel, D., Tonina, D., Bailey, P., Wright, C. W., Bohn, C., and Nayegandhi, A.: Remote sensing of channels and riparian zones with a narrow-beam aquatic-terrestrial LIDAR, Remote Sens., 1, 1065–1096, https://doi.org/10.3390/rs1041065, 2009.

Merwade, V., Cook, A., and Coonrod, J.: GIS techniques for creating river terrain models for hydrodynamic modeling and flood inundation mapping, Environ. Model. Softw., 23, 1300–1311, https://doi.org/10.1016/j.envsoft.2008.03.005, 2008.

Meyer, J. L., Sale, M. J., Mulholland, P. J., and Poff, N. L.: Impacts of climate change on aquatic ecosystem functioning and health, JAWRA J. Am. Water Resour. Assoc., 35, 1373–1386, https://doi.org/10.1111/j.1752-1688.1999.tb04222.x, 1999.

Pan, Z., Glennie, C., Hartzell, P., Fernandez-Diaz, J. C., Legleiter, C., and Overstreet, B.: Performance assessment of high resolution airborne full waveform LiDAR for shallow river bathymetry, Remote Sens., 7, 5133–5159, https://doi.org/10.3390/rs70505133, 2015.

Pan, Z., Glennie, C. L., Fernandez-Diaz, J. C., Legleiter, C. J., and Overstreet, B.: Fusion of LiDAR orthowaveforms and hyperspectral imagery for shallow river bathymetry and turbidity estimation, IEEE T. Geosci. Remote Sens., 54, 4165–4177, https://doi.org/10.1109/TGRS.2016.2538089, 2016.

Passalacqua, P., Belmont, P., Staley, D. M., Simley, J. D., Arrowsmith, J. R., Bode, C. A., and Wheaton, J. M.: Analyzing high resolution topography for advancing the understanding of mass and energy transfer through landscapes: A review, Earth-Sci. Rev., 148, 174–193, https://doi.org/10.1016/j.earscirev.2015.05.012, 2015.

Philpot, W.: Airborne Laser Hydrography II, https://doi.org/10.7298/jxm9-g971, 2019.

Pike, R. J.: The geometric signature: quantifying landslide-terrain types from digital elevation models, Math. Geol., 20, 491–511, https://doi.org/10.1007/BF00890333, 1988.

Pike, R. J.: A bibliography of terrain modeling (geomorphometry), the quantitative representation of topography, USGS Open-File Report, 02-465, https://doi.org/10.3133/ofr02465, 2002.

Quadros, N. D., Collier, P. A., and Fraser, C. S.: Integration of bathymetric and topographic LiDAR: A preliminary investigation, Int. Arch. Photogramm. Remote Sens. Spatial Inf. Sci., 37, 1299–1304, available at: https://www.isprs.org/proceedings/xxxvii/congress/8_pdf/13_ths-19/01.pdf (last access: 11 March 2026), 2008.

Rezende, I., Fatras, C., Oubanas, H., Gejadze, I., Malaterre, P. O., Peña-Luque, S., and Domeneghetti, A.: Reconstruction of effective cross-sections from DEMs and water surface elevation, Remote Sens., 17, 1020, https://doi.org/10.3390/rs17061020, 2025.

Richards, K. S.: Rivers: Form and Process in Alluvial Channels, Methuen, London, https://doi.org/10.4324/9781003465799, 1982.

Schwanghart, W. and Scherler, D.: Short communication: TopoToolbox 2 – MATLAB-based software for topographic analysis and modeling in Earth surface sciences, Earth Surf. Dynam., 2, 1–7, https://doi.org/10.5194/esurf-2-1-2014, 2014.

Shaker, A., Yan, W. Y., and LaRocque, P. E.: Automatic land-water classification using multispectral airborne LiDAR data for near-shore and river environments, ISPRS J. Photogramm. Remote Sens., 152, 94–108, https://doi.org/10.1016/j.isprsjprs.2019.04.005, 2019.

Sheffer, N. A., Enzel, Y., Benito, G., Grodek, T., Poart, N., Lang, M., Naulet, R., and Coeur, D.: Paleofloods and historical floods of the Ardèche River, France, Water Resour. Res., 39, https://doi.org/10.1029/2003WR002468, 2003.

https://doi.org/10.5194/egusphere-2026-724
Preprint. Discussion started: 31 March 2026

Simpson, G. and Schlunegger, F.: Topographic evolution and morphology of surfaces evolving in response to coupled fluvial and hillslope sediment transport, J. Geophys. Res.-Solid Earth, 108, https://doi.org/10.1029/2002JB002162, 2003.

Stammberger, V., Jacobs, B., and Krautblatter, M.: Hyperconcentrated flows shape bedrock channels, Commun. Earth Environ., 5, 184, https://doi.org/10.1038/s43247-024-01353-3, 2024.

Steinbacher, F., Dobler, W., Benger, W., Baran, R., Niederwieser, M., and Leimer, W.: Integrated full-waveform analysis and classification approaches for topo-bathymetric data processing and visualization in hydroVISH, PFG J. Photogramm. Remote Sens. Geoinf. Sci., 89, 159–175, https://doi.org/10.1007/s41064-021-00150-3, 2021.

Szafarczyk, A. and Toś, C.: The use of green laser in LiDAR bathymetry: State of the art and recent advancements, Sensors, 23, 292, https://doi.org/10.3390/s23010292, 2022.

Tarolli, P.: High-resolution topography for understanding Earth surface processes: Opportunities and challenges, Geomorphology, 216, 295–312, https://doi.org/10.1016/j.geomorph.2014.03.008, 2014.

Tonina, D., McKean, J. A., Benjankar, R. M., Wright, C. W., Goode, J. R., Chen, Q., Reeder, W. J., Carmichael, R. A., and Edmondson, M. R.: Mapping river bathymetries: Evaluating topobathymetric LiDAR survey, Earth Surf. Proc. Land., 44, 507–520, https://doi.org/10.1002/esp.4513, 2019.

Tsakiris, G. P. and Loucks, D. P.: Adaptive water resources management under climate change: an introduction, Water Resour. Manag., 37, 2221–2233, https://doi.org/10.1007/s11269-023-03518-9, 2023.

Van den Berg, J. H.: Prediction of alluvial channel pattern of perennial rivers, Geomorphology, 12, 259–279, https://doi.org/10.1016/0169-555X(95)00014-V, 1995.

Wagner, W., Ullrich, A., Melzer, T., Briese, C., and Kraus, K.: From single-pulse to full-waveform airborne laser scanners: Potential and practical challenges, Int. Arch. Photogramm. Remote Sens., XXXV, 201–206, 2004.

Wang, C. K. and Philpot, W. D.: Using airborne bathymetric lidar to detect bottom type variation in shallow waters, Remote Sens. Environ., 106, 123–135, https://doi.org/10.1016/j.rse.2006.08.003, 2007.

Wang, C., Li, Q., Liu, Y., Wu, G., Liu, P., and Ding, X.: A comparison of waveform processing algorithms for single-wavelength LiDAR bathymetry, ISPRS J. Photogramm. Remote Sens., 101, 22–35, https://doi.org/10.1016/J.ISPRSJPRS.2014.11.005, 2015.

Wang, D., Xing, S., He, Y., Yu, J., Xu, Q., and Li, P.: Evaluation of a new lightweight UAV-borne topo-bathymetric LiDAR for shallow water bathymetry and object detection, Sensors, 22, 1379, https://doi.org/10.3390/s22041379, 2022.

Wolman, M. G. and Miller, J. P.: Magnitude and frequency of forces in geomorphic processes, J. Geol., 68, 54–74, https://doi.org/10.1086/626637, 1960.

Yao, W. and Stilla, U.: Mutual enhancement of weak laser pulses for point cloud enrichment based on full-waveform analysis, IEEE T. Geosci. Remote Sens., 48, 3571–3579, https://doi.org/10.1109/TGRS.2010.2047109, 2010.

Yang, D., Qiu, H., Hu, S., Pei, Y., Wang, X., Du, C., and Cao, M.: Influence of successive landslides on topographic changes revealed by multitemporal high-resolution UAS-based DEM, Catena, 202, 105229, https://doi.org/10.1016/j.catena.2021.105229, 2021.

Zhao, X., Xia, H., Zhao, J., and Zhou, F.: Adaptive wavelet threshold denoising for bathymetric laser full-waveforms with weak bottom returns, IEEE Geosci. Remote Sens. Lett., 19, https://doi.org/10.1109/LGRS.2022.3141057, 2022.